Effect of the inclination angle on the transient melting dynamics and heat transfer of a phase change material

Santiago Madruga[1, a)] and Jezabel Curbelo[2]
[1)] *Departamento de Matemática Aplicada a la Ingeniería Aeroespacial, ETSI Aeronáutica y del Espacio, Universidad Politécnica de Madrid (UPM), Plaza Cardenal Cisneros 3, 28040 Madrid, Spain*
[2)] *Departamento de Matemáticas, Universidad Politécnica de Cataluña, Avda. Diagonal 647, 08028 Barcelona, Spain*

(Dated: 26 April 2021)

We report two-dimensional simulations and analytic results on the effect of the inclination on the transient heat transfer, flow, and melting dynamics of a Phase Change Material within a square domain heated from one side. The liquid phase has Prandtl number $Pr = 60.8$, Stefan number $Ste = 0.49$ and Rayleigh numbers extend over eight orders of magnitude $0 \leq Ra \leq 6.6 \cdot 10^8$ for the largest geometry studied. The tilt determines the stability threshold of the base state. Above a critical inclination, there exists only a laminar flow at the melted phase, irrespective of the Rayleigh number. Below that inclination, the base state destabilizes following two paths according to the inclination: either leading to a turbulent state for angles near the critical inclination or passing through a regime of plume coarsening before reaching the turbulent state for smaller angles. We find that the Nusselt and Reynolds numbers follow a power law as $Nu \sim Ra^{\alpha}$, $Re \sim Ra^{\beta}$ in the turbulent regime. Small inclinations reduce very slightly α and strongly β. The inclination leads to subduction of the kinematic boundary layer into the thermal boundary layer. The scaling laws of the Nusselt and Reynolds numbers and boundary layers are in agreement with different results at high Rayleigh convection. However, some striking differences appear as the stabilization of turbulent states with further increasing of the Rayleigh number. We find as well that the turbulent regime exhibits a higher dispersion in quantities related to heat transfer and flow dynamics on smaller domains.

I. INTRODUCTION

Phase Change Materials (PCM) exploit the latent heat of phase change to store large amounts of heat during its fusion or release it to its environment during the inverse solidification process. Historically, they have been a subject of interest in engineering due to their usage in thermal energy storage and management[1,2]. However, the behaviour of the liquid phase has received considerably less attention in the fluid dynamics literature despite the close relations with the classic problem of Rayleigh-Bénard convection (RB). Thus, it has been found how PCM melted from below can reach a turbulent state with similar scaling laws for the Nusselt number ($Nu \sim Ra^{0.29}$) and thermal and kinematic boundary layers ($\delta_T/h \sim Ra^{-0.29}$ and $\delta_u/h \sim Ra^{-0.16}$ respectively) as in high Rayleigh convection despite the different transition to turbulence and moving domain[3].

The inclination of the domain changes the symmetries of the flow and alters the heat transfer and flow dynamics rectangular enclosures heated from one side filled with PCMs of moderate to high Prandtl numbers (paraffin, lauric acid, or n-octadecane) shows no tilt for optimum heat transfer[4–9]. These works have been carried out only for a small set of inclinations, usually in steps of 45° or 30°, without enough resolutions to discern the effect of small inclinations. More involved configurations with homogeneous heating in the enclosure show $\theta = 60°$ as the optimum angle[10], or configurations with a constant flux of heat on a side in experiments to cool photovoltaic cells show $\theta = 45°$ as the optimum angle[11] within a set of three angles. In simulations with a very low Prandtl, as in gallium melting, no inclination has been as well reported as favourable[12].

The scarcity of works on inclined PCM melting contrasts with the interest in heat transfer and flow dynamics in tilted geometries in the closely related Rayleigh-Bénard problem. It has been found that in horizontal heating ($\theta = 90°$), as opposed to vertical heating ($\theta = 0°$), there is not a closed relation between kinematic and thermal dissipation with the Nussetl, Rayleigh and Prandtl numbers[13]. Convection in the presence of melting shares that feature at any tilt, as discussed next in the text. The effect of the inclination on the heat transfer and dynamics of convective flows have been measured and simulated mainly in rectangular and cylindrical geometries. Experiments and direct numerical simulation (DNS) of turbulent thermal convection for low Prandtl fluids shows that the highest heat transfer occurs after setting a large-scale circulation flow through the inclination of the cell. This inclination

[a)] Electronic mail: santiago.madruga@upm.es

does not correspond to the classic cases of vertical or horizontal heating. Furthermore, for low $Pr \lesssim 1$ this angle provides a single maximum for $Nu(\theta)$, and for greater inclinations, $Nu(\theta)$ exhibits a monotonous decay[14–18]. At intermediate and high Pr, the influence of the tilt on the heat transfer seems to be more involved. Increasing the tilt pushes the turbulent threshold to higher Ra at high Prandtl numbers[19]. Thus, while a similar relation between Nu and tilt has been found at $Pr \sim 4.3$[20] or $Pr = 7$[17], other authors report a monotonous decrease of Nu with increasing the inclination in rectangular cells for $Pr = 6.3$[21] and $Pr = 10$[22]. In experiments and simulations at high Prandtl, $Pr \sim 480$ contained in a quasi-two-dimensional square cell with $Ra \sim 10^8$ or $Ra \sim 5 \cdot 10^8$,[23] finds as well that $Nu(\theta)$ is maximum for $\theta > 0°$ but with two local maxima. In cylindrical geometries,[19] covers a wide range of Prandtl numbers $Pr \in [0.1 - 100]$ in a set of DNS for inclinations $\theta \in [0° - 90°]$ and $Ra \in [10^6 - 10^8]$. They find a dependence of Nu with the small inclinations for large Pr (decrease) and small Pr (increase).

The transient melting problem studied in this work generates a reduction of the aspect ratio Γ (ratio of distances between conductive walls and transversal direction) of the melted phase up to $\Gamma = 1$ for complete melting. It is interesting to observe that the aspect ratio also influences the heat transfer features in RB. Thus 2D (two-dimensional) simulations in rectangular geometries at $Pr = 0.71$, $Ra = 10^7$ and $\theta \in [0° - 180°]$ show that only for $\Gamma \leq 4$ exists an inclination $\theta > 0°$ with maximum Nu, and a monotonous decrease of Nu with the tilt for higher aspect ratios[24].

The effect of the inclination on the Reynolds number (Re) is another topic of interest. There are much fewer studies than on Nusselt number, and we are not aware of research on the effect of the inclination on the Reynolds number in melting PCM. DNS in cylinders with $\Gamma = 1/5$ filled with fluids at $Pr = 0.1$, 1 and $Ra \in [10^6 - 10^9]$[15] finds a tilt that maximizes the Reynolds number. While the behaviour is the same as for Nu, the maximum value of Re occurs at lower inclinations. It is worth noticing that they report a case for $Ra = 10^8$ and $Pr = 1$ where $Re(\theta)$ decays monotonously, as what we find in this work. Other works with DNS report as well an increase of Re up to a global maximum, followed by a gradual decrease in a wide range of Pr[19]. The aspect ratio Γ influences as well the behaviour of Re with the inclination. Thus[24] report minimal changes in Re for small inclinations, and only an apparent decrease of Re for $\theta > 25°$ for $\Gamma \leq 4$. For $\Gamma \geq 8$, they find a local minimum and maximum. Interestingly, several definitions of the Reynolds using different speeds in experiments at $Pr = 0.7$ in Ref.[21] reveal an increase of Re up to a global maximum, followed by a decaying trend at higher inclinations. As noticed before, this departs from the $Nu(\theta)$ relation observed in the same work. At high Pr,[23] finds that Re increases with θ up to a maximum corresponding to a small tilt to later drop rapidly. Also, they find a scaling $Re \sim Ra^{1/2}$ in agreement with Prandtl-Blasius laminar boundary layer theory. We will discuss as well how the definition of Re is relevant to characterize the effect of the inclination, and how the inclination leads to a trend of decaying Re for the melting PCM.

This article is structured as follows. We present the momentum and energy equations governing the PCM evolution in Section II. Besides, the balance equations for the kinematic and thermal dissipation rates are shown in Section III. A brief sketch of the numeric methods with convergence criteria is provided in Section IV. The results in Section V are organized in subsections on the angle of inclination, dynamic melting regimes, overall liquid fraction, storage of energy, Nusselt and Reynolds numbers, kinematic and thermal boundary layers. Finally, conclusions are discussed in Section VI.

II. PHYSICAL SETUP AND GOVERNING EQUATIONS

The PCM is enclosed in four squares of length $L = 4$, 6, 8 and $10\,cm$. A conductive boundary is held at constant temperature $T_h = 353.15\,K$, and the rest are adiabatic. The PCM used is n-octadecane, because it is one of the most studied PCM in thermo-regulation and energy storage applications with very well-known thermo-physical properties, due to the phase change taking place at room temperature and good stability properties. The Prandtl number of the liquid phase is $Pr = 60.8$ and the Stefan number $Ste = c_l\,(T_h - T_l)/\delta h = 0.49$, where δh is the latent heat, and c_l, T_l are the specific heat of the liquid phase and liquidus temperature, respectively.

The PCM is initially in solid form held at an uniform temperature $T_i = 298.15\,K$, and the phase change occurs in a tight range of temperatures between solidus $T_s = 298.65\,K$ and liquidus $T_l = 299.65\,K$. The simulations use, for the solid and liquid phases, the thermo-physical properties listed in Table 1 of[25].

The vertical axis of the cartesian domain is aligned with the gravity vector, and the angle θ corresponds to the angle formed by the horizontal axis with the conductive wall. The domain is inclined from $\theta = 0°$ up to $\theta = 180°$ in steps of $\Delta\theta = 5°$. Finer steps in the inclination $\Delta\theta = 1°$ are employed around $\theta = 0°$ to analyze in more detail the effect of the inclination over the reference of vertical heating.

The momentum and energy equations used to simulate the PCM are derived in the solidification literature and are outlined below. They are thoroughly discussed in[26–28].

A. Momentum equation

We consider a two-dimensional and incompressible flow where, for simplicity, viscous dissipation is neglected. We also assume that the solid and liquid phases are in local thermal equilibrium.

Within the range of temperatures considered, it is assumed that all physical properties are constant except the density in the buoyancy term (Boussinesq approximation). The momentum equation reads:

$$\rho\left[\frac{\partial \mathbf{u}}{\partial t}+(\mathbf{u}\cdot\nabla)\,\mathbf{u}\right]=-\nabla p+\mu\nabla^2\mathbf{u}-\rho\,g\,[1-\alpha(T-T_{ref})]\,\hat{\mathbf{e}}-Da\mathbf{u}, \tag{1}$$

being ρ the density, μ the dynamic viscosity, g the gravity acceleration, T_{ref} a reference temperature, α the thermal expansion coefficient, and $\hat{\mathbf{e}}=(\sin\theta,\cos\theta)$ a unit vector. The term Da generates a diffusive interface between the solid and liquid phases of the PCM. This Darcy term is added to use (1) in the whole domain, thus avoiding the burden of tracking the solid/liquid interface when fluid motion is present[26,27,29]. The functional form is model dependent, and the Carman-Kozeny equation for porous media $K(f)=\frac{\delta+f^3}{C(1-f)^2}=1/Da$ is the most frequent election in the PCM literature. This term is zero at the liquid phase, damps the velocity strongly within the mushy region, and suppress the velocity at the solid phase. Here, f is the volume fraction of melted PCM in a control volume of PCM and gives the porosity of the Carman-Kozeny equation, and δ is a tiny constant without physical meaning $\delta\ll 1$ to avoid division by zero. We choose $C=1.6\cdot 10^6 kg\,m^{-3}\,s$, in compliance with previous works[3,30]. Notice that the Darcy constant is a parameter that can be estimated through experimental tracking of the position of the solid/liquid interface along the time[31].

B. Energy equation

The thermal energy of the system reads as a function of temperature, assuming the same density in solid and liquid phases, as follows:

$$\left[\frac{\partial}{\partial t}+\mathbf{u}\cdot\nabla\right](C_p\,T+\delta h\,f)=\nabla(\lambda/\rho\nabla T) \tag{2}$$

where the specific heat $C_p=(1-f)c_s+f\,c_l$, and conductivity $\lambda=(1-f)\lambda_s+f\,\lambda_l$ are averaged by the contribution of the solid (subscript s) and liquid (subscript l) phase and δh is the latent heat of the solid/liquid transition of the PCM.

C. Coupling between Phase Change and Momentum Equation

The liquid fraction f allows the coupling of equations (1) and (2). The field f is modelled by a linear function of the temperature between the temperature of the solid phase T_s and the temperature of the liquid phase T_l as follows

$$f=\begin{cases}0 & if \quad T\le T_s\\ 1 & if \quad T\ge T_l\\ (T-T_s)/(T_l-T_s) & if \quad T_s<T<T_l\end{cases} \tag{3}$$

Notice that the temperature field rules the solid/liquid transition. The global liquid fraction $f_l=(\int f d\,\Omega)/\Omega$, frequently used in the thermal storage literature, provides the overall ratio between the volume of PCM in the liquid phase and the volume of the whole domain Ω.

III. BALANCE EQUATIONS

Averaging the equation for the conservation of kinematic energy over the whole domain at time t leads to the balance equation

$$\epsilon_u = \beta\, g\, (\sin\theta \langle T\, u\rangle_\Omega + \cos\theta \langle T\, v\rangle_\Omega) - \langle \partial_t \left(\frac{1}{2} U^2\right)\rangle_\Omega + \langle Da\, U^2\rangle_\Omega \tag{4}$$

where $\epsilon_u = \frac{\nu}{2}\langle \left|\nabla \mathbf{u} + \nabla \mathbf{u}^T\right|^2\rangle_\Omega$ is the kinematic dissipation rate and $\nu = \mu/\rho$ the kinematic viscosity. The brackets $\langle\cdot\rangle_\Omega$ correspond to the spacial average over the domain indicated at the subscript.

Furthermore, multiplying the energy equation by T we obtain the mean temperature fluctuation balance

$$\epsilon_T = \frac{1}{L\, H} \int_{\partial\Omega} (C_p\, T + \delta h\, f)\, \lambda/\rho\, \partial_n T\, ds - \frac{1}{2}\langle \partial_t \left(C_p\, T + \delta h\, f\right)^2\rangle_{LH} \tag{5}$$

where $\epsilon_T = \langle \lambda/\rho \nabla T \nabla \left(C_p\, T + \delta h\, f\right)\rangle_{LH}$ is a modified thermal dissipation rate (by a factor c_l^2 in absence of phase change), and the domain is supposed to be rectangular with L the length of the conductive side, and H the thickness.

There are two distinctive differences relatives to the classic Rayleigh-Bénard problem. Firstly, the problem is transient; there is not an average in the long-time limit that suppresses the temporal term. Secondly, the presence of the latent heat term modifies the thermal dissipation rate. Notice that without phase change, this term disappears, C_p becomes the constant c_l, and the dissipation term becomes the same as in the classic RB problem.

For the case of a conductive bottom with $T = T_h$ and $T_h > T_l$, and adiabatic top wall, the balance equation (5) simplifies to

$$\epsilon_T = \frac{\lambda_l/\rho}{H} \langle \partial_y T\rangle_{y=0} \left(c_l\, T_h + \delta h\right) - \frac{1}{2}\langle \partial_t \left(C_p\, T + \delta h\, f\right)^2\rangle_{LH} \tag{6}$$

where $\langle\cdot\rangle_{y=0}$ is the spacial average along the plane $y = 0$.

The evolution equation for the mean temperature provides more insights into the differences with the RB problem

$$\rho \partial_t \left(\langle C_p\, T + \delta h\, f\rangle_{LH}\right) = -\frac{1}{H}\int \partial_y J\, dy = -\frac{\lambda_l}{H}\langle \partial_y T\rangle_{y=0} \tag{7}$$

where $J(y) = \langle \rho\, v\, (c_p\, T + L\, f) - \lambda \partial_y T\rangle_y$ is the vertical heat flux averaged on a horizontal plane at height y. Thus the vertical flux $J(y)$ is not constant along the vertical coordinate, which is a fundamental difference with respect to Rayleigh-Bénard. The lack of constancy prevents a closure relation for the kinematic and thermal dissipation with the Nusselt number as in relations developed by[32], even for the transient case.

The velocity fields are null at the solid phase, and the adiabatic walls remove the thermal gradients in the solid phase, reducing the integration domain from the whole domain to the evolving region with $T > T_l$ for the computation of the kinematic and thermal dissipation rates. Thus it is possible to study the melting dynamics in the natural domain of melted PCM:

$$\epsilon_u = \beta\, g\, (\sin\theta \langle T\, u\rangle_m + \cos\theta \langle T\, v\rangle_m) - \langle \partial_t \left(\frac{1}{2} U^2\right)\rangle_m + \langle Da\, U^2\rangle_m \tag{8}$$

$$\epsilon_T = \frac{\lambda_l/\rho}{h} \langle \partial_y T\rangle_{y=0} \left(c_l\, T_h + \delta h\right) - \frac{1}{2}\langle \partial_t \left(C_p\, T + \delta h\, f\right)^2\rangle_m \tag{9}$$

where the integral averages are calculated over the melted region (subscript m), and h is the average thickness of the melted PCM. No conservation of the heat flux makes relevant the plane where the flux is measured to report the results. We choose the conductive plate at this work.

IV. NUMERICAL METHODS

To solve the equations of the model outlined in Section II, we use the open-source software OpenFOAM[33], based on finite volumes.

The model equations are integrated in time employing a second order Crank-Nicolson scheme with variable time step limited by a CFL condition.

We use a second-order upwind scheme to discretize the convective terms. Following[34], the source term in (2) is linearized as a function depending on temperature by split it in an explicit and implicit part (zero and first-order term, respectively). The liquid fraction is updated at every iteration, and a Rhie-Chow interpolation avoids

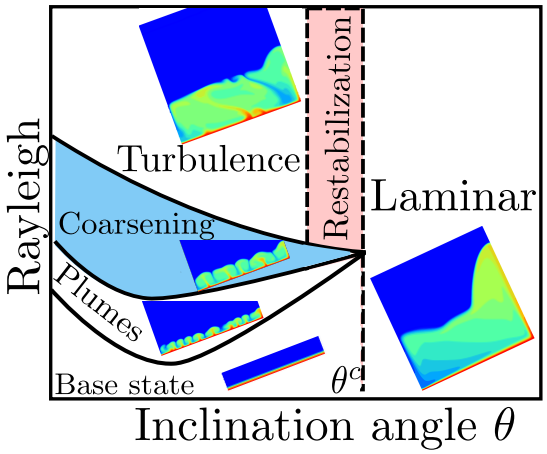

FIG. 1. Sketch of the different regimes of the melted phase as a function of the inclination and Rayleigh number. For inclinations above θ^c there is a laminar flow. For $\theta \leq \theta^c$ the melted phase can be, depending on the Rayleigh number, in a base state, plume growth regime, coarsening plumes regime, turbulent regime, or a laminar regime after a restabilization of the turbulent regime.

checkerboard solutions. The PIMPLE algorithm (see[35]) is used to solve the momentum and continuity equations because it ensures a right pressure-velocity coupling by combining PISO and SIMPLE algorithms.

In previous experimental and numerical works[25,29,36] the model has been validated, and the implementation of the bulk equations have been widely verified in different geometries (circular and rectangular domains). The code is stable and accurate and can model the strong coupling between energy and momentum equations typical of phase change problems in a wide range of Stefan numbers.

Regarding the spatial discretization, an uniform and structured mesh of different number of cells is used depending on the domain size. For domain size $L = 0.04m$ and $L = 0.06\,m$, we use 600×600 cells and 800×800 cells for $L = 0.08$ and $0.1\,m$.

This provides the largest grid size for $L = 0.1\,m$ with $1.25 \cdot 10^{-4}\,m$ and smallest grid for $L = 0.04\,m$ with $6.7 \cdot 10^{-5}\,m$. These grid resolutions resolve the Kolmogorov scale $\eta_k = \nu^{3/4}/\epsilon_u^{1/4}$ and the more demanding Batchelor scale relevant at high Prandtl numbers $\eta_b = \eta_k(t)/\sqrt{Pr}$. Here η_k is the minimum value reached by the Kolmogorov scale up to complete melting of the PCM for all the angles $\eta_k = min_{\theta\in[0,\pi]}(\eta_k(t))$ (η_k decreases from $8.5 \cdot 10^{-4}$ at $L = 4\,cm$ up to $7.6 \cdot 10^{-4}$ at $L = 10\,cm$). η_k corresponds to angles near $\theta = 90°$, and for turbulent behaviour that appears at lower inclinations it increases to $\eta_k \sim 10^{-3}$.

In addition to the validation with experimental and numeric works of the code, we also check that the input energy into the system $E_{input}(t) = \int_0^t \left(\int_0^L \lambda_l \langle T_y \rangle_{y=0}\, dx \right) dt'$ agrees with the change of enthalpy of the system with differences lower than 0.1%. Furthermore, we compute the LHS and RHS of the balance equation (7) to verify that both terms are numerically coincident along the time for $\theta \in [0, \pi]$.

V. RESULTS

Two parameters determine the main dynamic regimes occurring during melting: the gap of the melted phase h and the inclination angle θ. Other factors, like the size of the domain L, affect the thresholds, but they serve secondary roles as advancing or delaying the main regimes. Figure 1 shows a conceptual diagram of the regimes of the melted phase according to the inclination and Rayleigh number that we will discuss along this section.

A. Angle of inclination

1. No inclination $\theta = 0°$

In a previous work[3] is described a sequence of four regimes during the melting of a layer of n-octadecane heated from below with horizontal periodic boundary conditions as time advances. The article identifies (i) a conductive regime with no fluid motion, (ii) a linear regime where, after the conductive layer destabilizes by a Rayleigh-Bénard

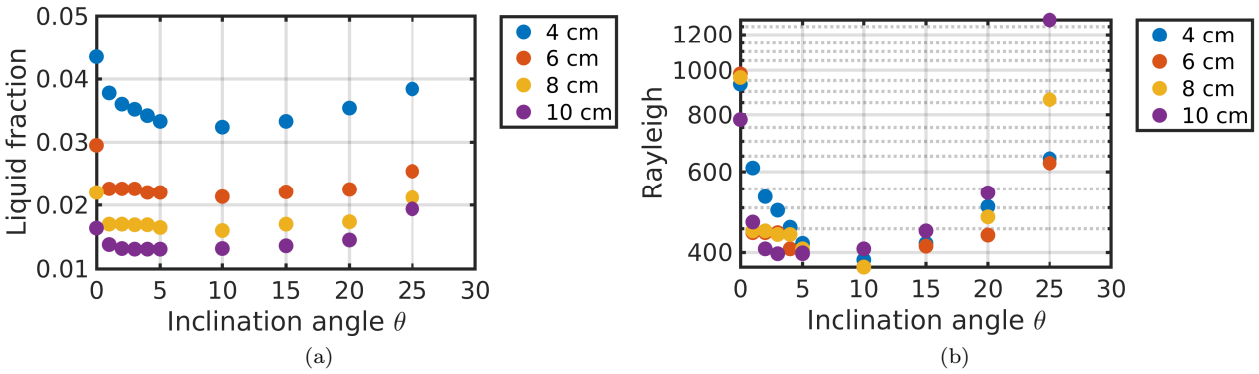

FIG. 2. The onset of the destabilization of the base state as function of the inclination (a) overall liquid fraction f_l, (b) Rayleigh number.

instability, thermal plumes appear and develop vertically (iii) a coarsening regime where these plumes destabilize and merge up to recover a similar aspect ratio to the cells at the onset of convection, and (iv) a final turbulent regime characterized by high deformation of the thermal boundary layer and the appearance of new plumes on the hot wall. These regimes are triggered by the increasing Rayleigh number resulting from the advancing of the solid/liquid interface, and a minimum thickness of the liquid phase is required to develop each one of them.

In this work, we use adiabatic boundary conditions on the vertical walls. At no inclination $\theta = 0°$, the secondary instability leads as well to the coarsening of plumes, but they become not ordered as happens with periodic boundary conditions. The rest of the regimes are similar to those described above for periodic boundary conditions.

2. Inclination $0 < \theta \leq \theta^c$

The inclination of the domain transforms the quiescent conductive regime into a base flow with a cubic shear velocity profile[37]. A single counterclockwise cell is formed within the liquid phase where the fluid moves up along the hot side and returns cooler along the solid/liquid interface. As the melted gap reaches a critical value, the base flow destabilizes and thermal plumes appear (for $\theta < \theta^c$ as discussed later). These plumes elongate during the linear regime, coarse and transition to turbulence for large enough domains.

The threshold of destabilization of the base flow depends on the inclination. Figure 2 shows the overall liquid fraction f_l and Rayleigh number at the onset of the destabilization of the base state. These values are calculated locating the origin of the growth stage of the thermal dissipation rate of the liquid phase ($\epsilon_T(T > T_l)$). The values of f_l and Ra at the threshold, $f_{l,c}(\theta)$ and $Ra_c(\theta)$ respectively, decreases up to an absolute minimum at $\theta \sim 10°$, and further inclinations lead to a monotonous increase of them up to $\theta = \theta^c$. Differences on the onset of destabilization among different sizes L are pronounced at small and large inclinations but becomes very small near the absolute minimum. While $Ra_c(\theta)$ is calculated from $f_{l,c}(\theta)$ and L the global liquid fraction provides a better representation of the onset of destabilization. The curves of $f_{l,c}(\theta)$ are well separated across the domain sizes L while the curves $Ra_c(\theta)$ cross between them. Bidimensional geometry in the simulations force rolls to be transversal to the inclination angle and the onset corresponds to the stability of transverse rolls[38–40].

Notice that figure 2 provides the beginning of the destabilization of the base state, not its complete replacement for thermal plumes, which takes further melting. Figure 3 shows a sequence of snapshots at the same time for $L = 4\,cm$ and $\theta = 0°, 5°, 10°, 15°, 20°, 25°$, where is observed how tilting the domain creates the plumes from the vertical walls (where the change of circulation of the base flow takes place). The figure also shows how the reminiscent base flow dominates the central region of the hot side, and how $\theta = 10°$ exhibits the fastest development of plumes.

3. Critical inclination θ^c

There exists a critical inclination θ^c where a global bifurcation of the flow occurs. It separates the region for multicellular flow $\theta \leq \theta^c$ from the region with laminar flow $\theta > \theta^c$, irrespective of the Rayleigh number. Up to θ^c, the base state becomes unstable with increasing Ra, above θ^c the base state is stable despite the high deformation

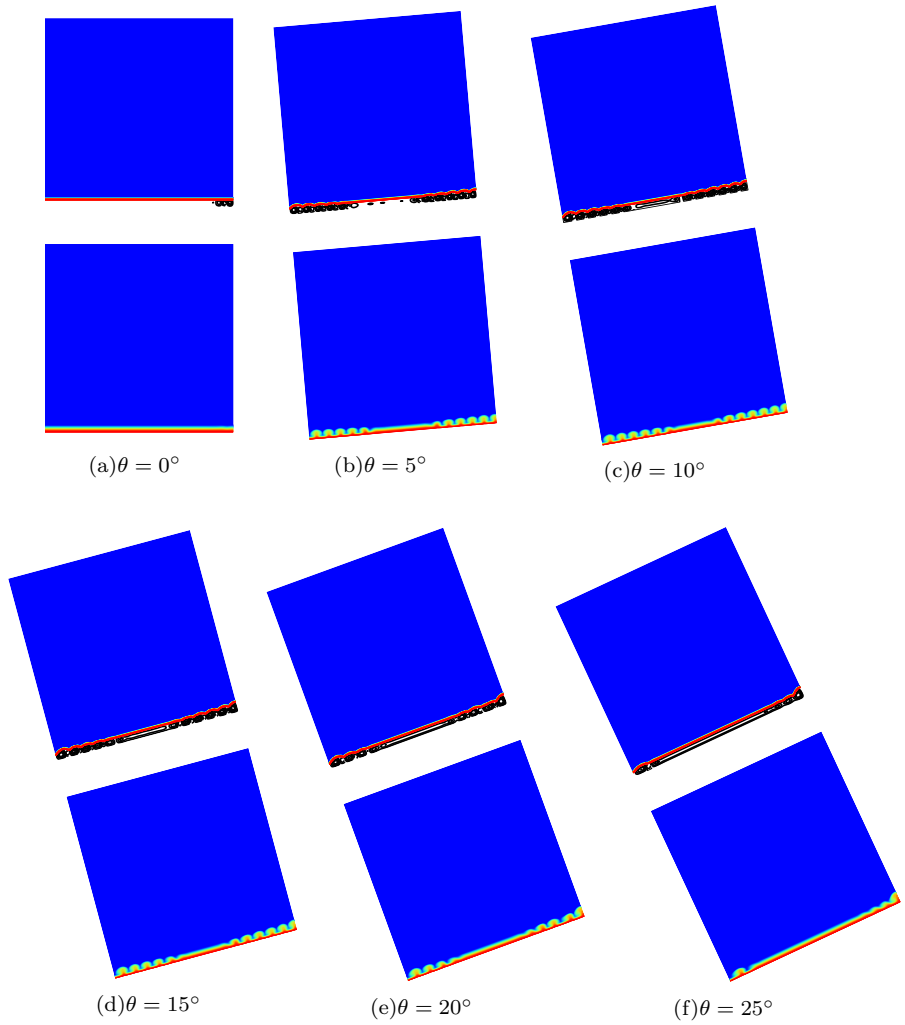

FIG. 3. Snapshots of the streamfunction (top) and temperature (bottom) fields at $t = 50\,s$ for $\theta = 0°(a), 5°(b), 10°(c), 15°(d), 20°(e), 25°(f)$ and $L = 4\,cm$.

of the solid/liquid interface characteristic of advanced melting. For $\theta > \theta^c$, a single plume develops with the stem on the right wall up to complete melting of the PCM.

The value of θ^c depends on the size of the domain. Thus we find $\theta^c = 29°$ for larger geometries, $L = 6$, 8, $10\,cm$, and a decrease for smaller domains, $\theta^c = 28°$ for $L = 4\,cm$, $\theta^c = 27°$ for $L = 2\,cm$, and $\theta^c = 23°$ for $L = 1\,cm$. The transition towards the laminar regime occurs through the progressive stability and widening of the base flow of the central region from the absolute minimum at $\theta \sim 10°$ up to θ^c.

The bifurcation angle θ^c splits the dynamics of melting in two regions with very different features. The global bifurcation at θ^c is observed in measurements related to heat flow, as Nu, and strength of fluid motions, as the Re. However, we will see as integral quantities frequently used in the PCM literature, such as the overall liquid fraction, are not suitable to detect the global bifurcation angle.

Since at $\theta = 180°$ only conductive heat transport occurs, there must be a transition or critical angle $0° < \theta < 180°$ that separates the turbulent from the laminar states even in the absence of phase change. Thus, in experiments with silicone oil at $Pr \sim 480$ and 2D DNS[23] find as well that at $\theta = 75°$ there is a change in the flow structure from turbulence to laminarity. In simulations at low Prandtl $Pr = 0.71$ in rectangular geometries with $\Gamma = 8$[24] shows a transition to laminar flow at $\theta = 140°$.

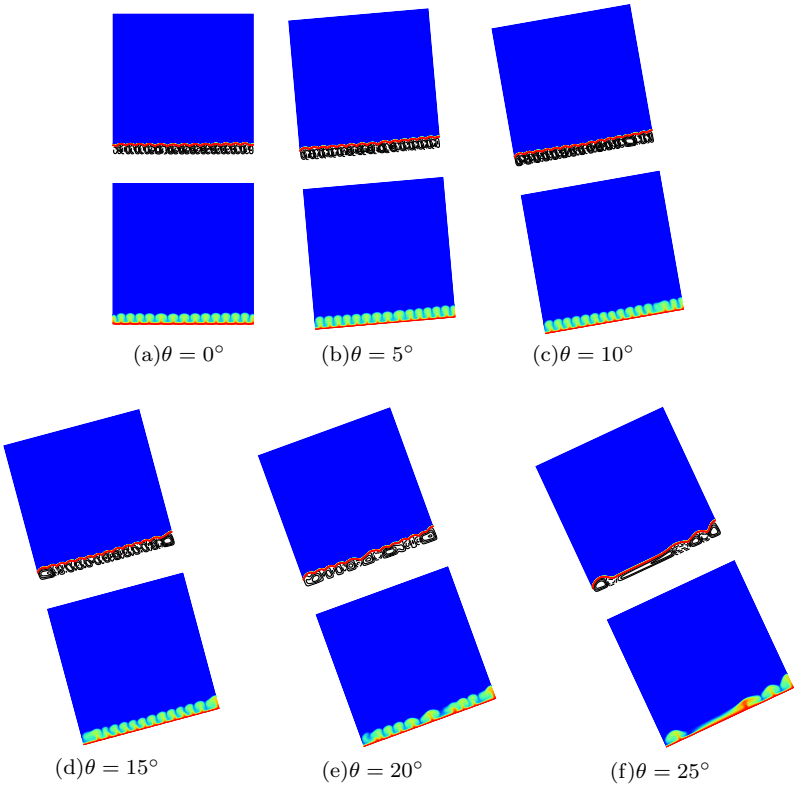

FIG. 4. Snapshots of the streamfunction (top) and temperature (bottom) fields at $t = 100\,s$ for $\theta = 0°(a), 5°(b), 10°(c), 15°(d), 20°(e), 25°(f)$ and $L = 4cm$.

B. Dynamic melting regimes

1. Destabilization of the base state

The destabilization of the base flow up to θ^c occurs through a RB instability. There is an ordered state of thermal plumes up to $\theta = 15°$ ($L = 4\,cm$) and non-equispaced plumes at higher inclinations (figure 4). Near θ^c, the plumes appear only in the proximity of the vertical walls, and the distance between them is very irregular (see figure 4(f)).

As the melting front advances, the plumes coarse, reducing their number and generally become not equidistant for $\theta > 0°$.

2. Secondary instability

Figure 5 shows a sequence of streamfunctions (top) and temperature fields (bottom) for $\theta = 0°, 5°, 10°, 15°, 25°$ at $t = 200\,s$. A secondary instability generates the coarsening of the plumes, excepting angles close to θ^c, such as $\theta = 25°$, where the hot side is not covered by plumes. Figure 6 shows the overall liquid fraction f_l and the Rayleigh number at the onset of the coarsening as a function of the inclination for $L = 4, 6, 8, 10\,cm$. We locate the destabilization of plumes tracking the onset of chaotic behaviour of the total flux integrated over the whole domain $\langle J_y \rangle$. We observe a general decay of the onset of the coarsening instability at small inclinations. However, the dispersion of values in the smaller geometries $L = 4, 6\,cm$ makes that decay with the inclination appears as a general trend, instead of monotonous decay. The largest domain $L = 10\,cm$ exhibits fastest onset of the coarsening with increasing inclination, and the rest of the domains at $\theta = 10°$, which corresponds to the inclination where first appear the thermal plumes. At fixed inclination, the secondary instability develops faster for larger sizes. Likewise to the first instability, the representation based on the overall liquid fraction provides more explicit information on the influence of the domain size. The coarsening of plumes can also be appreciated in streamlines and temperature fields during melting in rectangular enclosures of PCMs with high Prandtl number, such as lauric acid, at 0° and 45°[6] and at 0° for finned enclosures[41], and very low Prandtl number such as gallium for 30° and 60°[12].

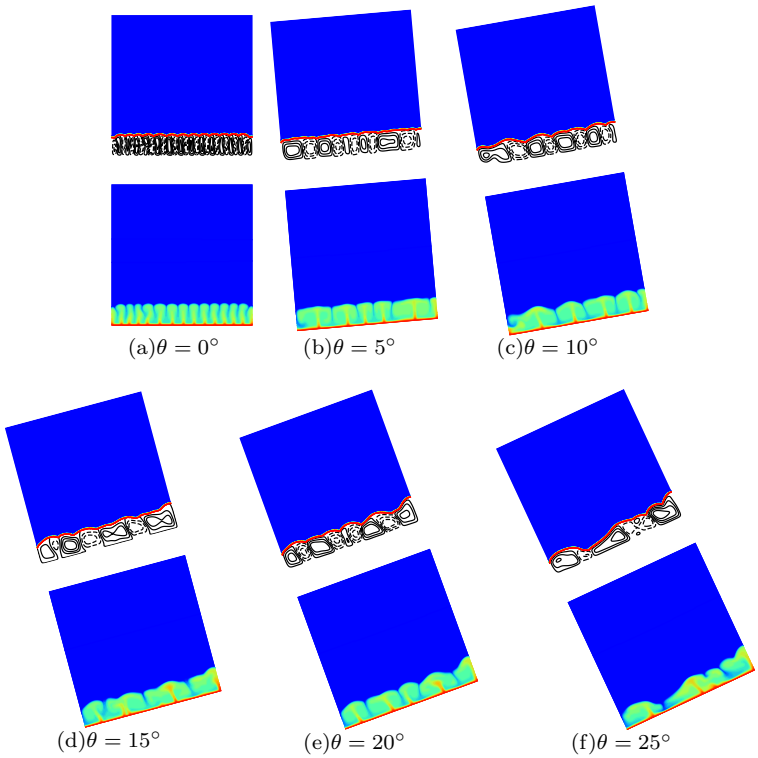

FIG. 5. Snapshots of the streamfunction (top) and temperature (bottom) fields at $t = 200\,s$ showing different stages of the coarsening of plumes after the secondary instability for$\theta = 0°(a), 5°(b), 10°(c), 15°(d), 20°(e), 25°(f)$ and $L = 4cm$.

We observed in a previous work[3] how the coarsening without inclination is independent of ΔT. The origin of this stability is the destabilization of the melted region that occurs when the density becomes unstably stratified. Figure 7 shows the normalized density $\rho/\rho_0 = 1 - \alpha(T - T_{ref})$ at $\theta = 0°$ and $\theta = 10°$ averaged on vertical planes as a function of the height over the hot wall. When the melted phase reaches a density profile completely stratified with layers of heavier PCM over lighter, the liquid phase destabilizes by buoyancy and the second instability is triggered.

3. Turbulent regime

As melting progress, and the gap of the liquid phase is large enough, a turbulent regime appears after the coarsening of plumes, or without that coarsening for angles near to θ^c. This regime is characterized by a high deformation of the thermal boundary layer on the hot wall and the emergence of new plumes from this side. The turbulent regime corresponds to the latest stage of melting, and notably most of the melting occurs within this regime for large enough domains.

Figures 8 and 9 show the temperature and velocity profiles at $t = 300\,s$ and $600\,s$, respectively. Deformation of the thermal boundary layer is small for $300\,s$ and pronounced for $600\,s$ with the emergence of some plumes in most of the angles at the latter time. This regime is similar to the turbulent state of high Rayleigh convection at high Prandtl numbers, as discussed in Subsec. V E-V G based on scaling arguments.

Interestingly, at some inclinations near θ^c there happens a substantial reduction of turbulent motions, or a transition to laminarity, after the solid/liquid interface at the right wall touches the top wall ($\theta = 15°$ at $L = 4\,cm$, $\theta = 15°, 20°$ at $L = 6\,cm$). Furthermore, we find a return to the laminar state even before the melting front reaches the top wall, neglecting the requirement of forcing boundaries to recover the stability. For instance, at $L = 4\,cm$ we find the return to the laminar state at $\theta = 20°$ and $\theta = 25°$. This result is very striking since it involves a turbulent motion that regains stability at higher Ra. The transition occurs through the merging of the convective cells up to the creation of a counterclockwise laminar flow. This process is illustrated in figure 10 in a sequence of snapshots of streamlines and temperature fields at different times. Notice that the recovery of stability at high Ra is only observed for angles close to θ^c, and the transition towards laminarity occurs at lower Ra for higher inclinations. Another instance of recovery of ordered states at higher Ra is found in non-Boussinesq convection, where hexagons

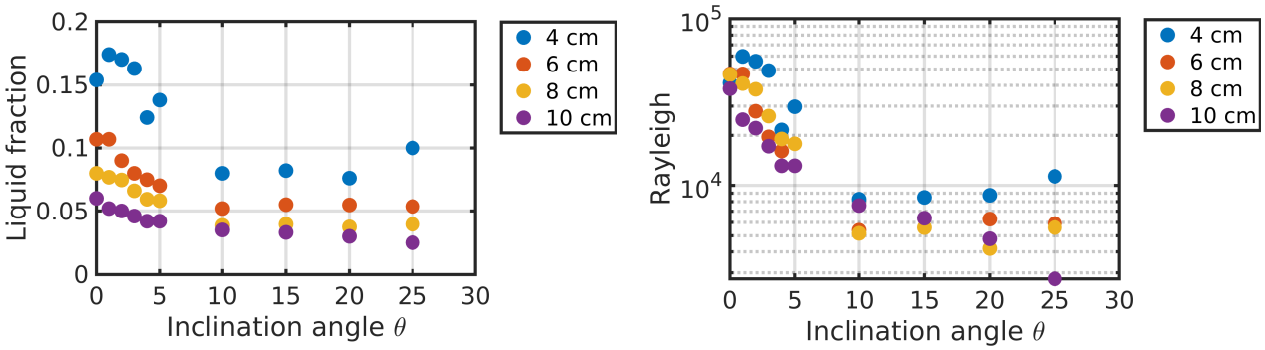

(a) (b)

FIG. 6. The onset of the plume coarsening as a function of the inclination: (a) liquid fraction (b) Rayleigh number.

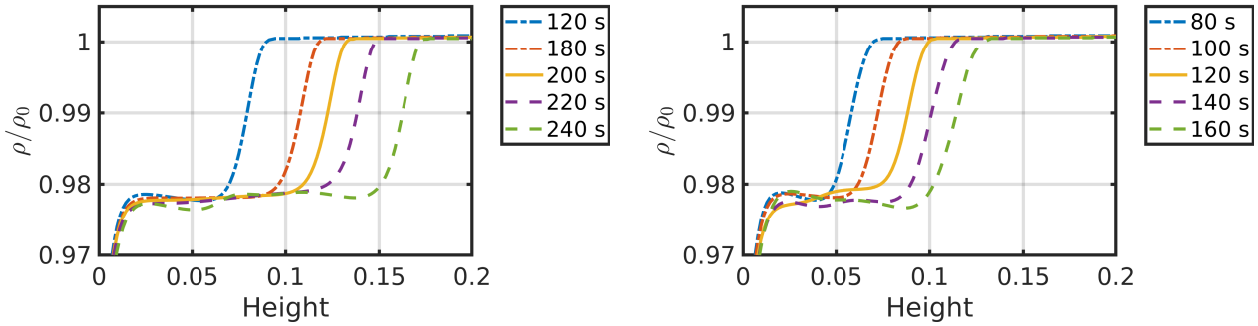

(a)$\theta = 0°$ (b)$\theta = 10°$

FIG. 7. Normalized density $\rho/\rho_0 = 1 - \alpha\,(T - T_{ref})$ averaged on horizontal layers over the hot wall at different times for $\theta = 0°$ (a) and $10°$ (b), and $L = 4\,cm$. The secondary instability is triggered when the whole density profile becomes unestably stratified.

reappear at a higher Rayleigh number after a disordered state[42].

C. Global liquid fraction

Figure 11 shows the global liquid fraction f_l as a function of the time. This integral quantity is commonly used to describe the thermal performance of PCM systems. The curves show a smooth evolution from no inclination at $\theta = 0°$ up to $\theta = 180°$, where only conductive heat transport occurs. The curves overlap up to the destabilization of the base state for $\theta \leq \theta^c$. Later they depart in two groups: (i) for $\theta \leq \theta^c$, they continue to be concave, and (ii) for $\theta > \theta^c$ they become convex until the melting front reaches the top wall, recovering the concavity after this merge.

Tracking the value of f_l when the melting front at the right wall reaches the top wall $f_{l,right}$ provides a clear picture of the different melting regimes. Thus figure 12 (circles) shows scattered values close to $f_{l,right} = 1$ up to $\theta = 5°$, and further inclinations within the turbulent regime show a monotonous decrease of $f_{l,right}$. From θ^c, there is a smooth decrease of $f_{l,right}$ up to $\theta = 90°$, which is the angle where the right wall melts the fastest. From this angle there is an increase of $f_{l,right}$ with the inclination, but from $\theta = 135°$ the dependence on the system size becomes very small due to the diminutive effects of convection in melting compared with conduction. Figure 12 shows as well ($\times$) the value of f_l at complete melting of the top wall $f_{l,top}$ and shows how for $\theta^c < \theta < 90°$ there is solid PCM constrained on the left wall and surrounded by liquid PCM.

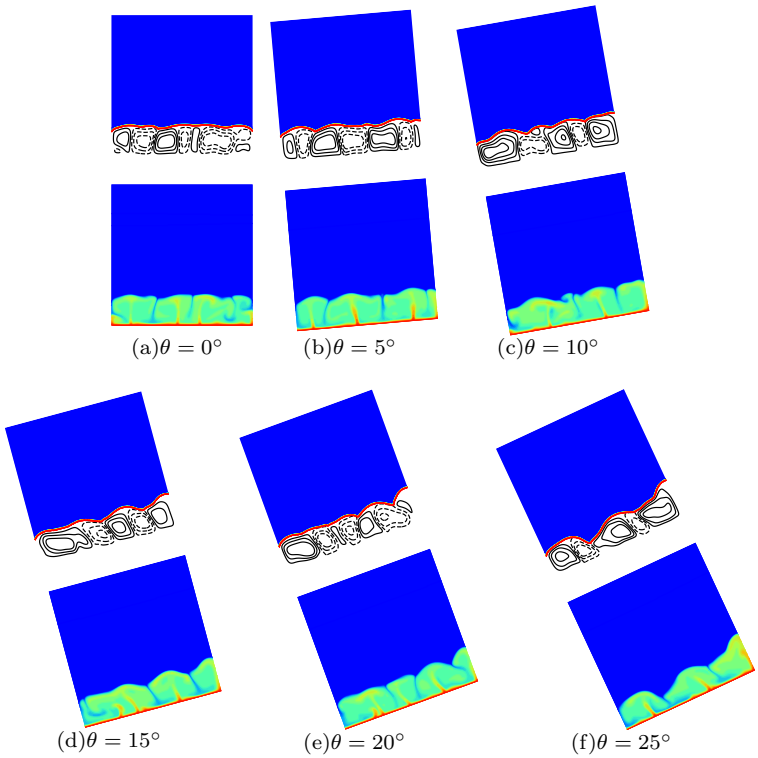

FIG. 8. Snapshots of the streamfunction (top) and temperature (bottom) fields at $t = 300\,s$ for $\theta = 0°(a), 5°(b), 10°(c), 15°(d), 20°(e), 25°(f)$ and $L = 4cm$.

The time for complete melting t_m is correlated with the melting regimes but not determined by them as seen in figure 13. The first regime of t_m ends at θ^c. Below this angle the presence of the turbulent regime and associated irregular melting front generate scattered values of total melting time t_m as a function of the inclination. The dispersion of melting times decreases for larger L. The reason is that more thermal plumes fit into the domain, and the corrugation of the solid/liquid interface is averaged and less influential on the time to complete melting. For tilts beyond θ^c, all the sizes exhibit a monotonous decrease of t_m from θ^c up to $\theta = 45°$, and a monotonous growth of t_m with the inclination from this minimum, shaping a jockey stick form. Thus within the laminar regime at $\theta > \theta^c$, we observe two opposed trends for t_m. Notice that the absolute minimum for t_m can be found at an angle below θ^c for domains large enough to develop a turbulent regime due to the corrugations of the melting front.

The global behaviour of t_m respect to θ exhibited in figure 13 shows a depression in the region $\theta < 45°$ for $L = 10\,cm$, which flattens progressively for smaller sizes, and for $L \leq 4\,cm$ this region changes of curvature making $\theta = 45°$ the absolute minimum. The curvature becomes more pronounced for lower sizes L (not shown).

D. Storage of energy

Figure 14(a) shows the total input of heat Q_m per unit of PCM mass ($K\,J/Kg$) required for complete melting as a function of the inclination. The total input of heat $Q_m(\theta)$ exhibits dispersed values in the turbulent regime, although there is trend upwards with the inclination. Beyond θ^c there is a monotonous increase of $Q_m(\theta)$ up to an absolute maximum at $\theta = 95°$, roughly $\sim 15\%$ higher than $Q_m(\theta = 0°)$. Beyond $\theta = 95°$, $Q_m(\theta)$ exhibits a monotonous decay with the inclination. The energy required for complete melting with no inclination is very close to the energy at $\theta = 180°$, where only melting through conduction takes place.

From θ^c, fixed the inclination, the energy per unit of mass increases slightly with the size L, about 0.2% between successive sizes L up to $\theta \sim 105°$. This weak dependence on size is due to the compensation of the higher input of heat in geometries with longer conductive walls with the need to move further the melting front to liquify the whole PCM. Notice that at the conductive limit of $\theta = 180°$, the same input energy is required for full melting in all L. It is especially meaningful for applications in thermal storage that the total energy per unit of mass harvested up to full melting depends much more strongly on the inclination of the enclosure than its size.

Figure 14(b) shows the total input of energy Q_m per unit of mass over the melting time t_m, which is a measure of

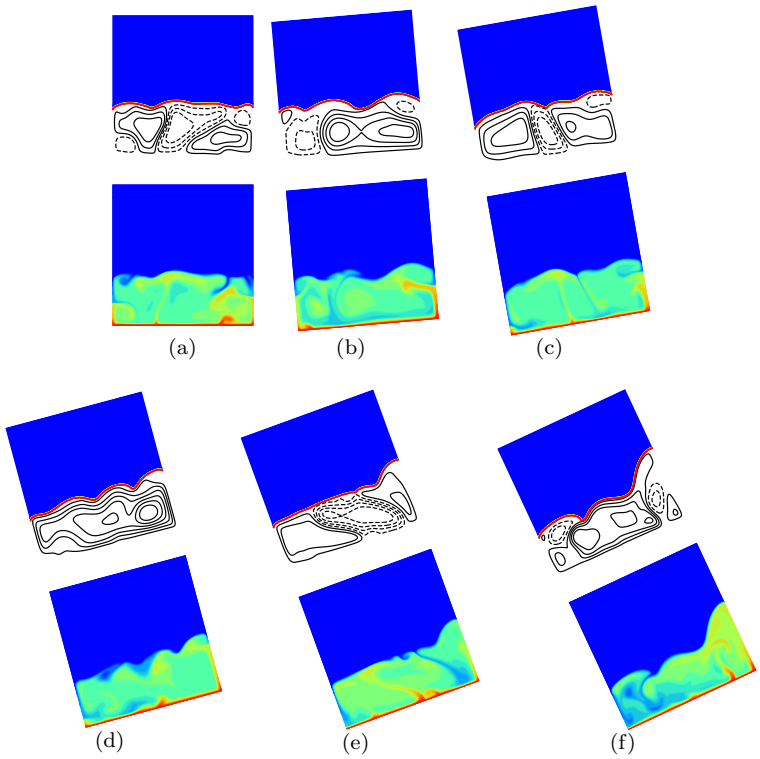

FIG. 9. Snapshots of the streamfunction (top) and temperature (bottom) fields at $t = 600\,s$ for $\theta = 0°(a), 5°(b), 10°(c), 15°(d), 20°(e), 25°(f)$ and $L = 4cm$.

the efficiency of the PCM to collect thermal energy. The greater variation of the melting time across the inclinations with respect to the input of energy, makes t_m dominate the ratio and provides the same information as figure 13: at large sizes L no or small inclinations are the most efficient, and for smaller L inclinations about $\theta = 45°$ are the most efficient. The progressive reduction of convective transport leads to a strong decay of the efficiency in energy harvesting from $\theta = 90°$, and the dominating conductive transport from $\theta = 135°$ makes these inclinations more than one order magnitude more inefficient than no inclination.

E. Nusselt and Rayleigh numbers

We employ an effective Rayleigh number in this work, defined using the averaged thickness of the solid/liquid melting interface h as

$$Ra = \frac{\rho\,\alpha\,\Delta T\,h^3\,g}{\mu\,\kappa_l} \tag{10}$$

where κ_l is the thermal diffusivity of the liquid phase $\kappa_l = \lambda_l/(\rho\,c_l)$ and $\Delta T = T_h - T_{top}$. In this definition, T_{top} is the melting front temperature $(T_l + T_s)/2$, or the weighted temperature between melting front and top adiabatic wall when the liquid phase partially covers the latter. Notice that with this definition, the value of Ra depends on the melting front position. Since the interface is diffuse, we choose the cells with liquid fraction $f_l = 0.5$ as the criterium for the thickness of the interface. This liquid fraction corresponds to the melting front temperature $(T_s + T_l)/2$.

The local Nusselt number is defined by $Nu_x = \frac{h}{T_h - T_m}\partial_y T|_{y=0}$. In this definition, due to the finite thickness of the interface, $Nu_x \neq 1$ when conduction prevails on the liquid phase. Henceforth, we will use the averaged Nusselt number along the hot wall $Nu = \frac{1}{L}\int_0^L Nu_x\,dx$ to discuss the results.

We discuss next, the Nusselt curves allow to distinguish clearly the turbulent regime with irregular oscillations (figures 15(a,b)) from the laminar regime with smooth curves (figures 15(c,d)).

The relation between the heat flux, represented by the Nusselt number, and strength of the convective motions, represented by the Rayleigh number, has been thoroughly studied in the high Rayleigh convection literature and shown to exhibit a power-law $Nu \sim Ra^{\alpha}$ in a wide range of Ra[43]. We observe as well this behaviour at the

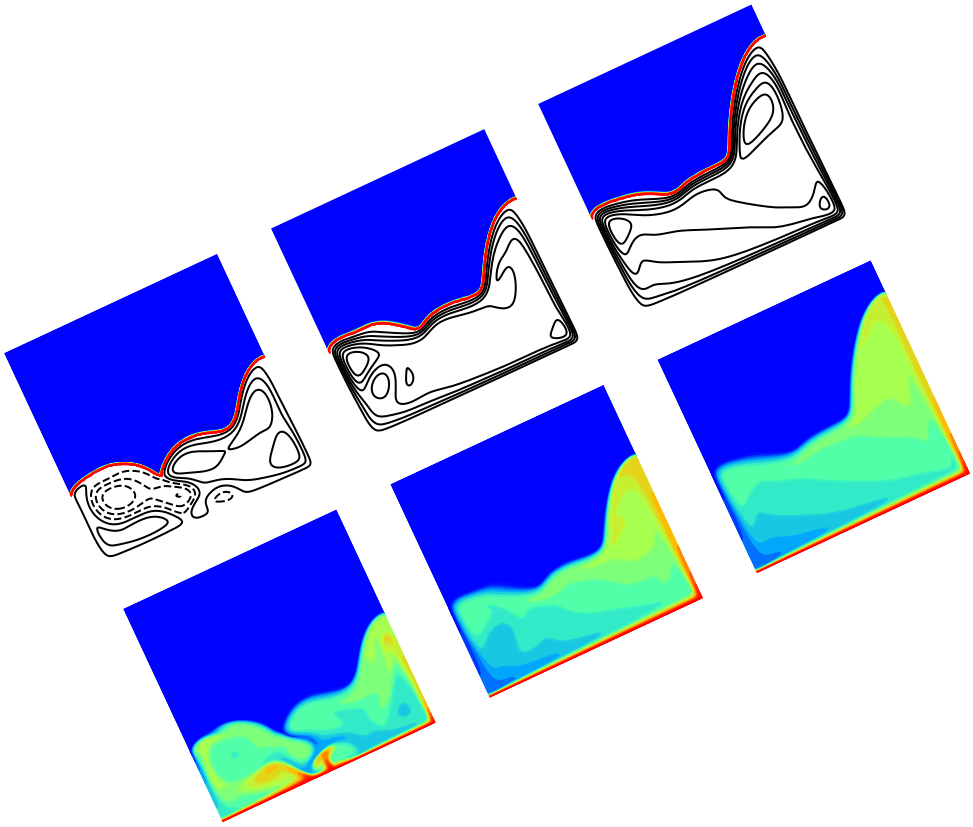

FIG. 10. Snapshots of the streamfunction (top) and temperature (bottom) fields at $t = 600, 800, 1000\,s$ for $\theta = 25°$ and $L = 4cm$. The fields show a re-stabilization of the turbulent dynamics at higher Ra.

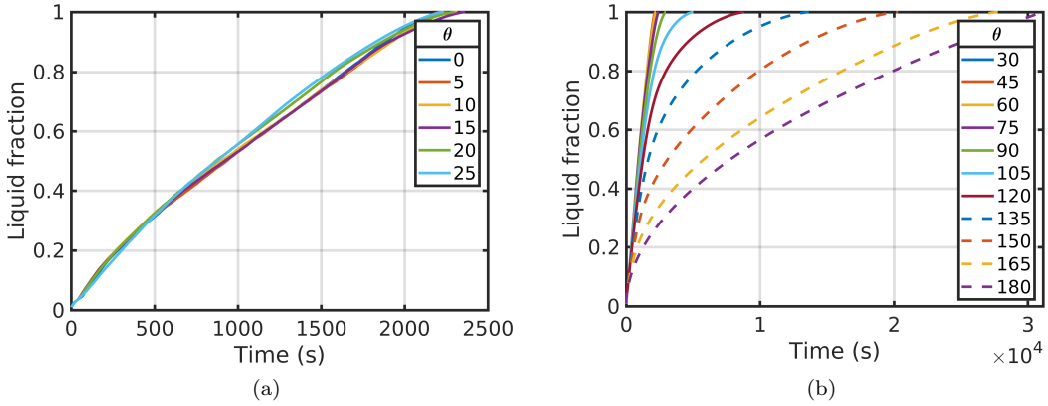

FIG. 11. Liquid fraction versus time for $4cm$: (a) $0 \leq \theta \leq 25°$, (b) $\theta \geq 30°$

turbulent regime during PCM melting. For vertical heating (no inclination), the average exponent is $\alpha \sim 0.29$ in n-octadecane melting[3], in agreement with theoretical predictions of $2/7$[32,44,45]. Also, it has been found in vertical heating of gallium that phase change induces a greater Nusselt number for small Rayleigh numbers[46]. Figure 15(b) shows the evolution of the Nusselt number as function of the Rayleigh number during melting in a log-log scale for $\theta < \theta^c$. Fluctuating curves at the turbulent regime overlap without a clear trend introduced by the inclination.

Figure 16(a) shows the exponent α as a function of the inclination for all the sizes. At the turbulent regime, the mean of this exponent is higher for larger L ($\overline{\alpha} = 0.3,\ 0.3095,\ 0.3128,\ 0.3149$ for $L = 4,\ 6,\ 8,\ 10\,cm$) However, at fixed L, there is not a univocal effect on the enhancement or suppression of the heat flux for small inclinations. This is observed in figure 16(b), which zooms the turbulent region and shows additional values of α for $\theta = 1°, 2°, 3°, 4°$.

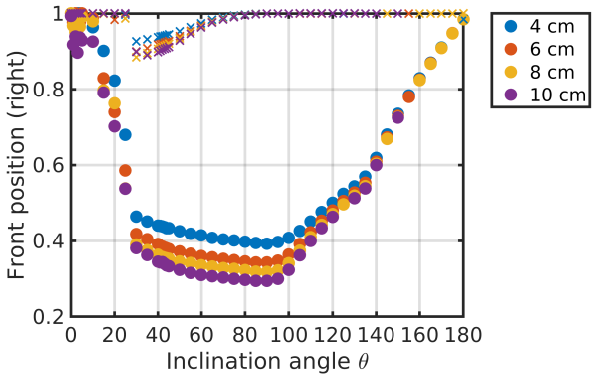

FIG. 12. Value of the overall liquid fraction at complete melting of the PCM on the right wall $f_{l,righ}$ (circles) and top wall $f_{l,top}$ ($\times$) as a function of the inclination.

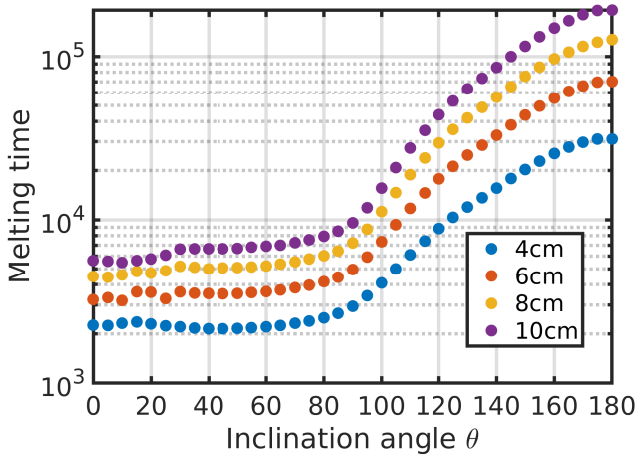

FIG. 13. Melting time as function of the inclination for $L = 4\,, 6\,, 8\,, 10\,cm$.

Most of the domains $L = 4, 6, 10\,cm$ exhibit a decay of the heat flux tilting the domain just $\Delta\theta = 1°$, however for $L = 8\,cm$ there is a minimal increase of the heat flux. From $\theta = 10°$ there is a clear increase of the heat flux with the tilt up to $\theta = \theta^c$. The dispersion of the values of α increases for lower L, as a consequence of greater influence of irregular interface deformations at these sizes, as discussed in Section V C.

Similarly to our results, some experiments in water with $Pr = 4.38$ in cylinders for $Ra = 1.8 \cdot 10^{10}$ and $7.2 \cdot 10^{1020}$ and $10^9 \leq Ra \leq 10^{1147}$ have found very small variation in Nu with respect to the vertical case for small inclinations. Also, experiments in rectangular cells with fluids of $Pr = 10$ at $Ra \sim 10^{1022}$ and $Pr = 6.3$ at $Ra \sim 10^{921}$ find small declines on the Nusselt number for small tilts. Other experiments covering a wide range of aspect ratios $\Gamma \in [1 - 6]$ and $Pr = 3$[48] find that heat transfer is not affected by tilting $\theta = 10°$ in spite of meaningful changes in the flow structure. Thus, our findings agree with a subset of works in the high Rayleigh literature that concludes that inclinations of small angles influence the heat transfer slightly while having a profound influence on the flow structure.

At the laminar regime $\theta > \theta^c$, there is a monotonous decay of the exponent α with the inclination. The exponent α is very similar for all the sizes up to $\theta = 90°$, with a small increase with L until this angle. There is a jump in α at the laminar regime with respect to the turbulent regime near θ^c. The highest values of α locate near θ^c. Notice that the exponents for the laminar regime have been obtained only in the region that follows a power law (maximum Rayleigh of this region decreases with the inclination, as shown in figure 15(d)), which covers progressively fewer decades of the Rayleigh number and loses significance for very high inclinations.

Within the laminar regime $\theta > \theta^c$ appear two sub-regimes for the heat flux: up to $\theta = 45°$ the Nusselt curves increase with the inclination: above $\theta = 45°$, the Nusselt curves decay monotonously with the inclination as a consequence of diminishing strength of convective motions. These trends are observed as well in the location of $max(Nu(\theta))$ that exhibits a maximum at $\theta = 45°$. This behaviour is appreciated more clearly in the curves of

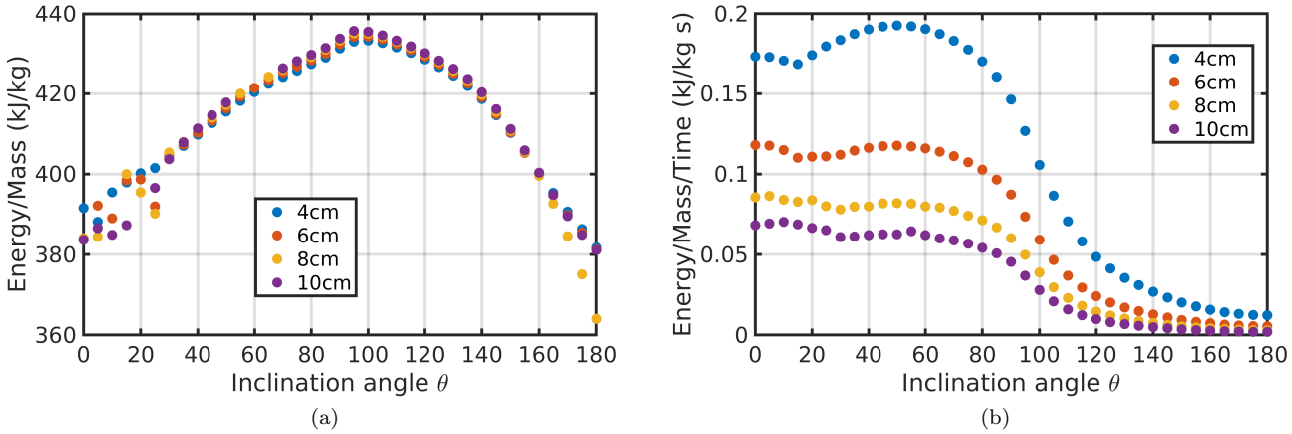

FIG. 14. (a) Total input of energy per unit of mass Q_m $(K\,J/Kg)$ up to complete melting of the PCM, and (b) input of energy over melting time Q_m/t_m $(K\,J/Kg\,s)$ as a function of the inclination for $L = 4\,,6\,,8\,,10\,cm$.

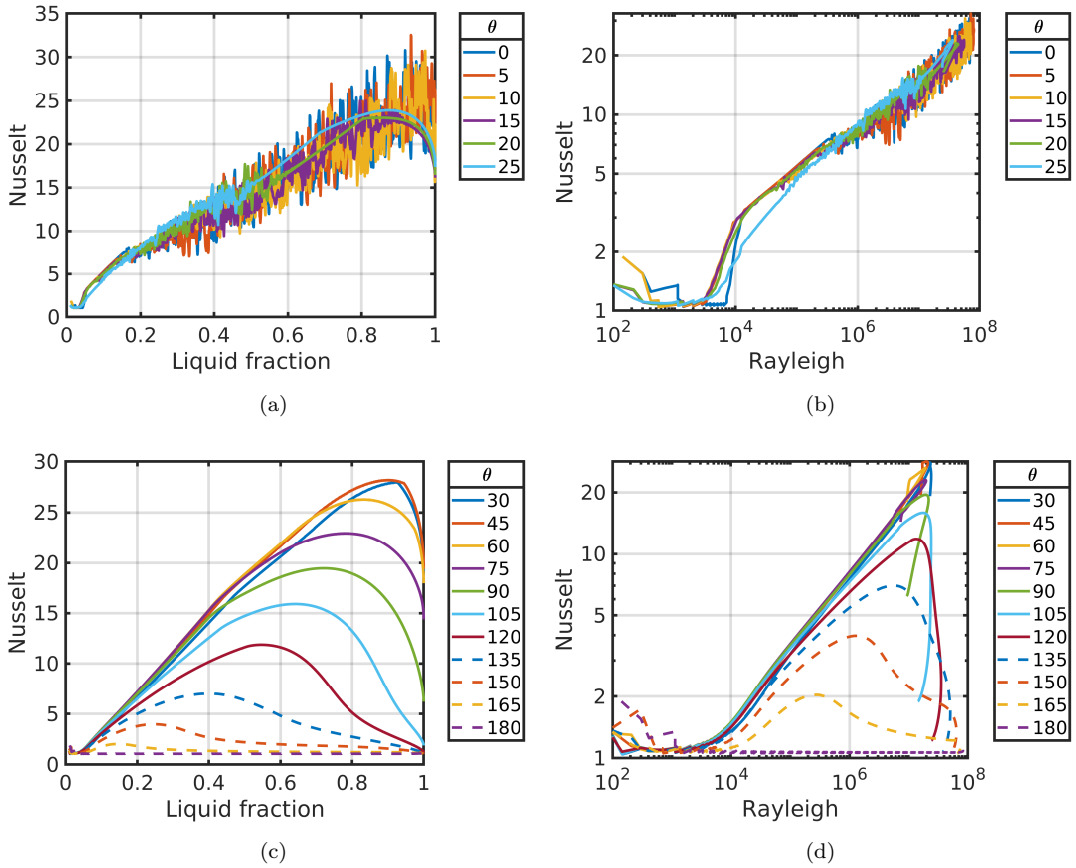

FIG. 15. Nusselt number with respect to the overall liquid fraction (left), Nusselt number with respect to the Rayleigh number (right) for domain size $L = 4\,cm$: (a) and (b) $0 \leq \theta \leq 25°$, (c) and (d) $\theta \geq 30°$

flux integrated along the whole domain $\langle \mathrm{J(y)} \rangle$ shown in figures 17(b,d). The flux $J(y)$ includes as well the vertical velocity and the curves around 45° surround the rest of the inclinations, exhibiting a maximum when the melting front reaches the top wall. At the turbulent regime, the flux curves exhibit as well a power-law relation with Ra (c.f. figure 17(c)), as shown in figures 17(b,d), with no significant differences at small inclinations. An interesting feature of the flux curves is that they explain the minimum of the melting time at $\theta = 45°$ as the inclination with the highest area under curve within the laminar regime ($\theta > \theta^c$).

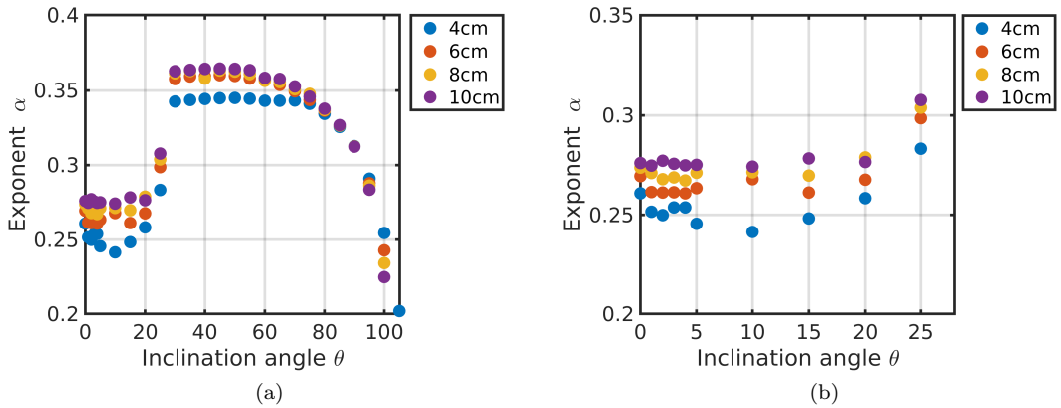

FIG. 16. (a) Exponent α of the relation $Nu \sim Ra^{\alpha}$ for domain sizes $L = 4, 6, 8, 10, cm$. (b) Close-up of (a) for $\theta \leq 25°$.

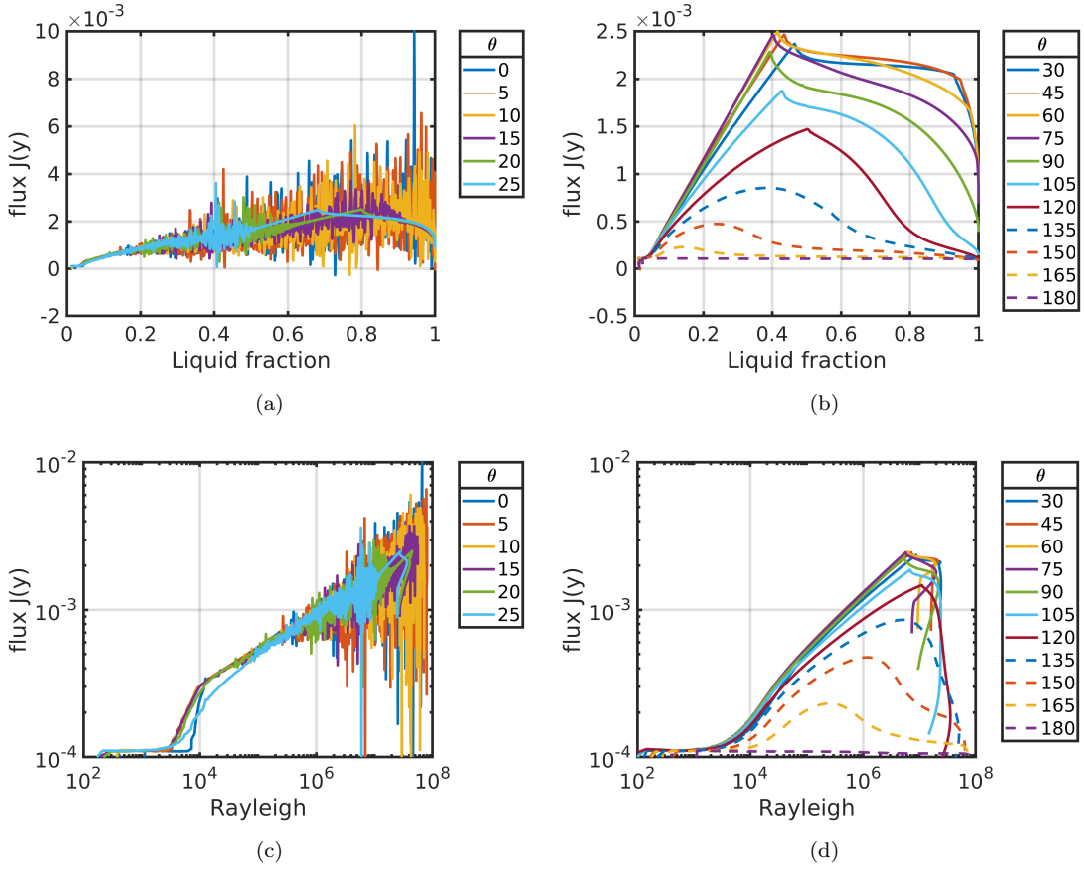

FIG. 17. Total Flux J(y) averaged versus liquid fraction f and Rayleigh number at $4cm$. (a,c) $0 \leq \theta \leq 25°$, (b,d) $\theta \geq 30°$.

DNS in cylinders at $Pr = 0.1, 1$[15], experiments in sodium[14,18], DNS and experiments in air in parallelepipeds[16], DNS in square cavities at $Pr = 7$[17], or at the turbulent regime in experiments and DNS at high Prandtl $Pr \sim 480$[23], find in common a $Nu(\theta)$ with a maximum at $0° < \theta < 90°$ and later a decay. We find this behaviour in the exponent α at the laminar regime, $\theta > \theta^c$, instead of the turbulent regime of those works.

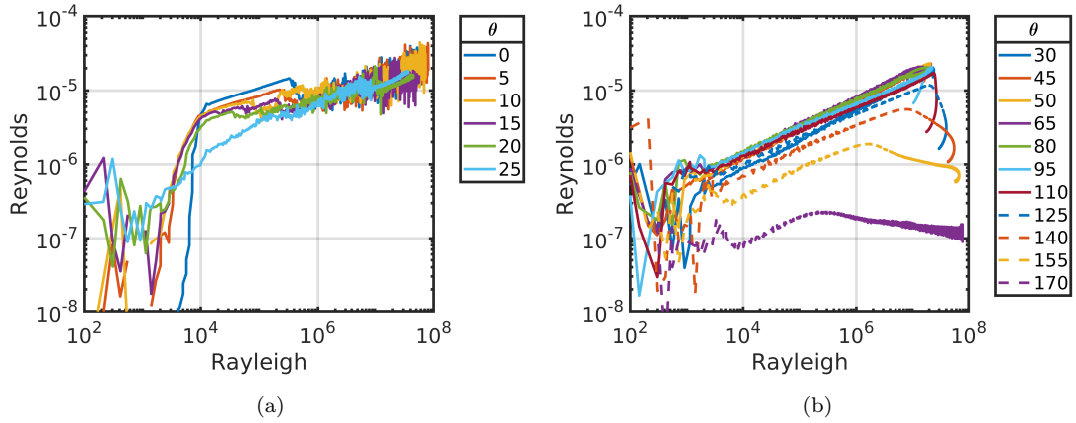

FIG. 18. Reynolds number based on the wing velocity definition Re_v as a function of the Rayleigh for (a) $0 \leq \theta \leq 25^\circ$ and (b) $30 \leq \theta \leq 170^\circ$ at $L = 4\,cm$.

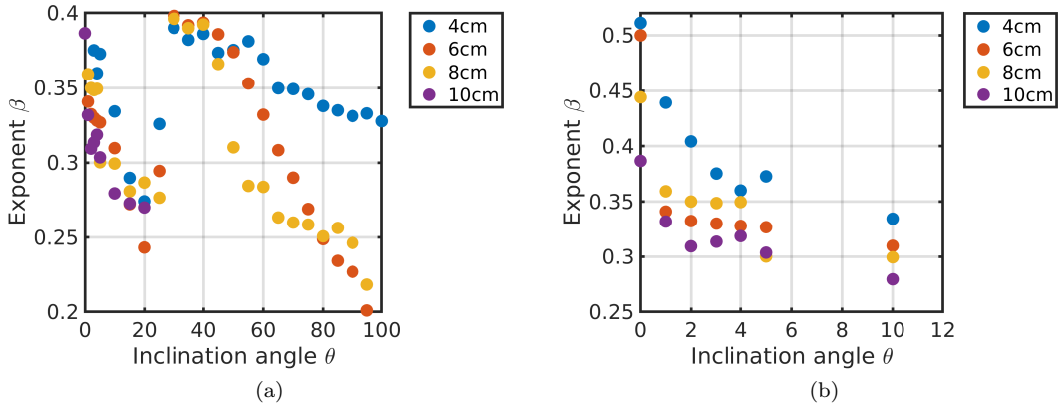

FIG. 19. (a) Exponent β of the relation $Re_v \sim Ra^\beta$ for domain sizes $L = 4$, 6, 8, $10\,cm$, respectively. (b) Close-up of (a) for $\theta \leq 10^\circ$.

F. Reynolds number

We have investigated two types of definitions of the Reynolds number. The first type corresponds to properties of the velocity field in the liquid phase, such as the Reynolds number related to the averaged module of velocity on the liquid phase $Re^U \equiv h\langle U\rangle_l/\nu$, or based in the maximum value of some velocity field $Re^{max|U|} \equiv h\ max|U|/\nu$, where U can be u, v, $\mathbf{u}$ or their modulus. The second type corresponds to definitions based on the wind velocity $Re_U \equiv h\,U_M/\nu$, where U is some velocity field, such as v, $|v|$, u, $|u|$, $|\mathbf{u}|$, and U_M is the maximum of $\langle U\rangle_y$, where $\langle\cdot\rangle_y$ is the spacial average across the horizontal line $y = cte$ (cf. figure 4 of[13]). The second definition can include in the average horizontal liquid and solid phases of the PCM.

At non-inclination, all those definitions allow to fit the turbulent regime to a power law. However, for increasing inclinations, there is a progressive bending of the curves in the log-log diagram (not shown). The departure from the power-law occurs at different angles according to the Reynolds definition; thus, $Re^{|\mathbf{u}|}$ exhibits a power-law until the melting front reaches the top wall, $Re^{|v|}$ exhibits still a power law in the turbulent regime up to $\theta \sim 10^\circ$. Reynolds based on vertical wind velocity Re_v exhibits a power law for a broader range of inclinations and very high Ra, extending even to the laminar regime, as shown in figure 18. Based on these observations, we choose the definition based on the wing velocity Re_v to study how it affects the Nusselt number.

Figure 19 shows the exponent β of the relation $Nu \sim Re_v^\beta$ as a function of the inclination for all the domains. It exhibits two remarkable differences with respect to the exponent α discussed in the previous section: the dispersion of β is greater than the dispersion of α, and there is not a direct relationship between size and value of β. This points towards the exponent α being a more robust quantity to characterize the dynamic regimes.

At the turbulent regime, the mean of the exponents $Re_v \sim Ra^\beta$ ($\overline{\beta} = 0.29$, 0.24, 0.23, 0.21 for $L = 4$, 6, 8, $10\,cm$,

respectively) exhibits an increasing trend for smaller domains L. Opposite to the Nusselt number, Reynolds decreases clearly as a consequence of inclining the domain. Figure 19(b), shows that Re_v decays with a small inclination $\Delta\theta = 1°$, and a general trend downwards by further augmenting the inclinations. A comparison of figures 19(b) and 16(b) up to θ^c shows that the inclination has a greater effect on diminishing the strength of the convective motions than on changing the strength of the flux of heat. The laminar regime $\theta > \theta^c$ exhibits a smooth downwards trend with increasing the inclination, as a consequence of the reduced strength of the convective motions at higher inclinations within the laminar regime. Similarly to the exponent α, the angles slightly above θ^c exhibit a strong increase of the exponent β with respect to the turbulent regime.

While at high Rayleigh convection frequently occurs a maximum of Re at a non-zero inclination in a wide range of Prandtl numbers[15,19,21,23], we find that the high dispersion of β and downtrend at $\theta < \theta^c$ does not favour an extreme value of Re. We notice, however, that other results in RB convection are similar to this work. Thus in a set of 2D DNS in rectangles at $Pr = 0.7$ and $Ra = 10^{7}$[24] report as well very slight changes in Re for small inclinations and a clear decrease of Re for $\theta > 25°$ for aspect ratios ≤ 4 with a definition based on $Re^{|\mathbf{u}|}$. Interestingly, experiments in water in cylindrical cells with aspect ratio $\Gamma = 1$ show and increase of Reynolds for small inclinations[47], and others experiments at $Pr = 5.3$ in a range $2.4 \cdot 10^8 \leq Ra \leq 5.6 \cdot 10^9$ and a narrow range of inclinations $0° \leq \theta \leq 3.4°$ by[49], show a similar exponent to this work using a definition of Reynolds as Re_U. They find $Re \sim Re^{-0.43}$, which is very close to our results for the largest geometries, and they find not extreme of Re_U either. However, notice that this work finds a strong decay of β in the same range of angles where[49] measure invariance with the inclination.

G. Thermal and kinematic boundary layers

The thickness of the thermal boundary layer δ_T, following[13], is the distance between the intersection of the tangent of the horizontally averaged temperature profile at the hot wall $\bar{T} = T_h + dT/dy|_{y=0}\, y$ with the mean temperature between the hot wall and the interface $T_m = (T_h + (T_s + T_l)/2)/2$. From this definition, and using the Nusselt number defined in Section V E, the thickness of the thermal boundary layer δ_T can expressed as well as

$$\delta_T = \frac{h}{2\,Nu} \tag{11}$$

The thickness of the boundary layer normalized by the gap of the melted phase as a function of Ra for inclinations lower than θ^c is provided in figure 20(a), and for higher inclinations in figure 20(b). For $\theta < \theta^c$ the curves follow a power law $\delta_T/h \sim Ra^{\alpha_T}$ since the destabilization of the base state, whose exponents are shown in figure 21(a). For $\theta < \theta^c$, the averaged value of the exponent $\alpha_T = -0.25 - 0.26, -0.27, -0.28,$ for $L = 4,\ 6,\ 8,\ 10\,cm$ decreases with the size L. For the laminar regime $\theta > \theta^c$, the exponents α_T vary smoothly with the inclination, with a minimum at $\theta = 45°$ and a monotonous increase for higher inclinations. In absolute value, they behave as the exponent α since they are derived from the Nusselt curves.

Following[13], we define the thickness of the kinematic boundary layer δ_u/h as the distance from the hot wall to the intercept of $\overline{u} = \frac{d\,\overline{u}}{d\,y}\Big|_{y=0} y$ and $\overline{u} = max(\overline{u})$, where $\overline{u}(y)$ is the spatial average along the horizontal axis of the module of the velocity. A detailed graphical representation of the kinematic and thermal boundary layers can be found in Figure 4 of Ref.[13].

The thickness of the kinematic boundary layer normalized by the gap of the melted phase is shown in figure 22(a) for inclinations below θ^c, and figure 22(b) for inclinations over θ^c. In opposition to the rest of the curves for $\theta < \theta^c$ as a function of Ra, such as Nusselt, flux, Reynolds, or thickness of the thermal boundary layer; there is a noticeable separation between $\delta_u/h(\theta)$ curves in the turbulent regime, with the slope decreasing progressively for higher inclinations. The trend continues for $\theta > \theta^c$ up to $\theta = 105°$, when the trend reverses in a region where the convective motions are very weak. Since the destabilization of the base state the curves follow a power law $\delta_u/h \sim Ra^{\alpha_u}$ for $\theta < \theta^c$, and for most of the range of Ra for $\theta > \theta^c$. The exponents α_u are shown in figure 21(b). The exponents decrease from $\alpha_u = -0.15$ at $\theta = 0°$ to $\alpha_u = -0.26$ at $\theta = \theta^c$ for $L = 4\,cm$. Similar number are found for the rest of the sizes given the scattered values and not clear dependence on L at this region. At the laminar region $\theta > \theta^c$ there is a monotonous decrease since from $\alpha_u = -0.26, -0.28, -0.27, -0.28$ up to $\alpha_u = -0.36, -0.37, -0.38, -0.38$ for $L = 4,\ 6,\ 8,\ 10\,cm$ respectively at $\theta = 105°$. Thus, the laminar region exhibits a a clear dependence on size with a decrease for higher L.

The boundary layers kinematic δ_u/h and thermal δ_T/h are superposed for $\theta = 0°$. However, the inclination progressively separates them. The separation becomes very noticeable since roughly $\theta = 10°$ and higher inclinations, where the kinematic boundary layer becomes contained within the thermal boundary layer $\delta_u/h < \delta_T/h$.

The scaling of the boundary layers in the presence of melting has received attention on the non-inclined RB literature for lateral periodic boundary conditions (c.f.[3]). This works finds similar values for α_T and α_u. The average scaling $\delta_u/h \sim Ra^{-0.29}$ does not agree with the exponent -0.25 predicted by the Prandtl-Blasius theory.

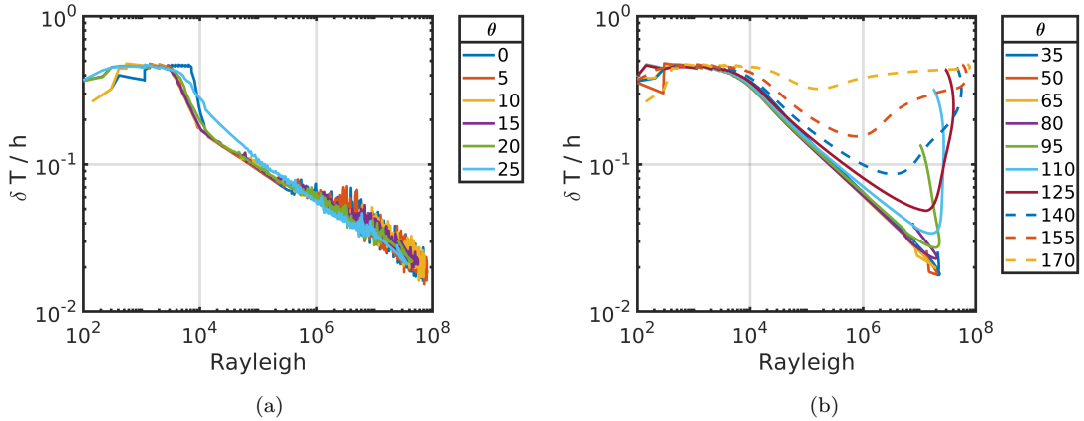

(a) (b)

FIG. 20. Thickness of the thermal boundary layer over melted gap as a function of Ra, δ_T/h vs Ra for $4cm$: (a) $0 \leq \theta \leq 25°$, (b) $\theta \geq 30°$.

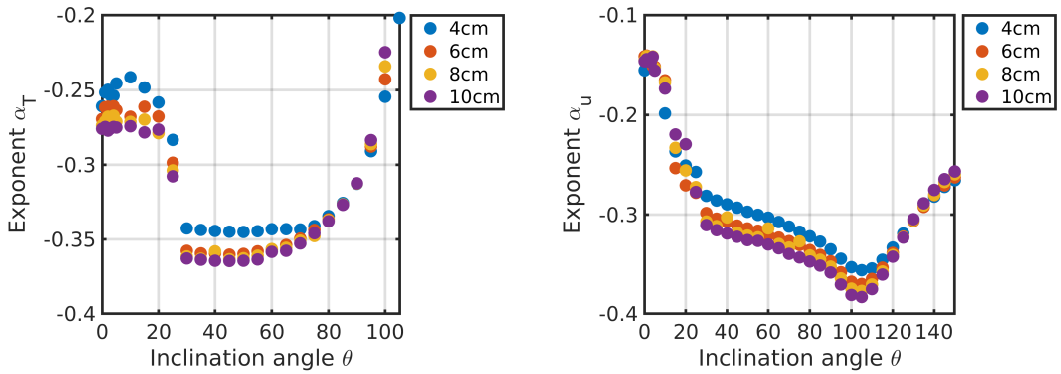

(a) (b)

FIG. 21. (a) Exponent α_T of the relation $\delta_T/h \sim Ra^{\alpha_T}$ and (b) exponent α_u of the relation $\delta_u/h \sim Ra^{\alpha_u}$ as a function of the inclination for $L = 4, 6, 8, 10\,cm$

No studies of these scalings are known to us in inclined convection coupled with phase change. On the other hand, while the scaling of boundary layers in RB is a common topic at non-inclination, it is comparatively much less studied in the presence of a tilt. Thus, in DNS for 3D rectangular geometries with horizontal heating ($\theta = 90°$) at low Prandtl $Pr = 0.709$ for $Ra \in [10^5 - 10^9]$ is found that boundary layer thickness for the temperature and velocity field comply with scalings of the Prandtl-Blasius-Pohlhaussen theory[13]. Interesting, the experiment in water by[49] reports for α_u a sharper decline with the inclination, from -0.19 at $\theta = 0.5°$ to -0.32 at $\theta = 3.4°$. Their value for $\theta = 0°$ is closer to Prandtl-Blasius than our results.

VI. CONCLUSIONS

We have studied the effect of the inclination on the melting dynamics of a PCM heated from below. The work studies systematically how the tilt affects metrics related to the performance of PCM systems, such as melting times or energy storage capacity, and quantities related to the dynamics of the melted phase of the PCM, such as the exponents of the Nu and Re relations with the Rayleigh number, or the thickness of the thermal and kinematic boundary layers.

The inclination generates two global regimes: (i) a multicellular regime for angles below a critical angle θ^c, and (ii) a laminar regime above θ^c. The first regime exhibits a sequence of states similar to melting with no inclination when time advances: (i) destabilization of the base flow, (ii) stable growth of thermal plumes, (iii) coarsening of plumes (for angles not very close to θ^c), and (iv) turbulent heat transfer (for large enough domains).

We find that the mechanism that leads to destabilization of the thermal plumes is a buoyancy-driven instability

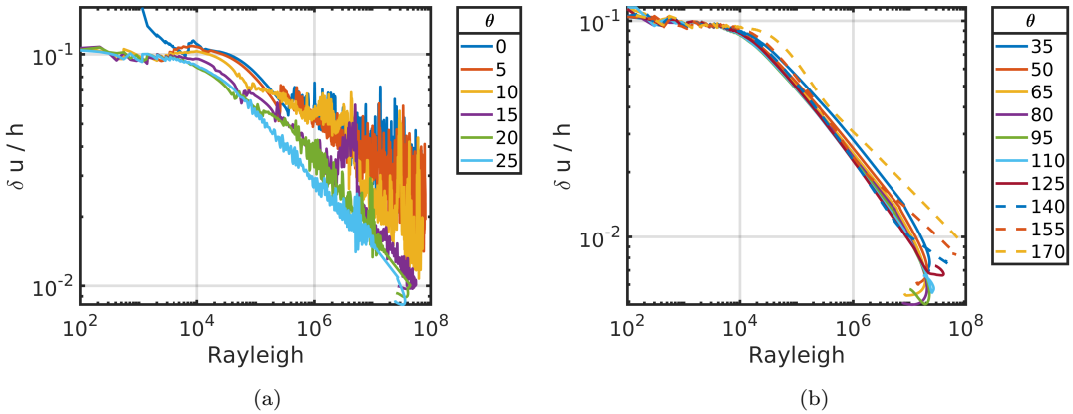

FIG. 22. Thickness of the kinematic boundary layer over melted gap as a function of Ra, δ_u/h vs Ra for $4cm$: (a) $0 \leq \theta \leq 25°$, (b) $\theta \geq 30°$.

that arises when the density of the melted PCM increases monotonously with the height. After this buoyancy induced destabilization appears a turbulent state.

An interesting finding is that the turbulent state can recover stability by further increasing the Rayleigh number. These restabilizations occur only at inclinations near the global bifurcation angle θ^c. After the restabilization, there is a return to the laminar flow with a very corrugated solid/liquid interface that remains up to complete melting of the PCM.

The presence of the turbulent regime in the liquid phase for $\theta \leq \theta^c$ is relevant on metrics related to heat transfer performance of the whole PCM. Thus the melting time is only slightly affected by small inclinations, but the effect is more irregular and profound for small geometries. In these, the strongly corrugated solid/liquid interface play an important geometric role in the filling of the square domains. Because of that, global measures like melting time or input of energy are more scattered at small sizes than in larger domains. For the named laminar regime $\theta > \theta^c$ all the measures evolve smoothly with the inclination angle. The optimum angle (fastest melting time) depends on the size of the system. For increasing domain sizes the curve of melting times as a function on the inclination flattens, and the optimum angle is at $\theta = 0°$ or close angles; however, for small $L \leq 4\,cm$ the region around 45° increases the curvature, and this local minimum becomes global and thus the optimum angle.

The input of thermal energy per unit of mass required to melt the PCM is very similar across all the geometries. It exhibits a dome form with a peak for $\theta = 95°$. Interestingly, the extreme cases: $\theta = 0°$, where convective motions are the strongest, and the conductive case at $\theta = 180°$ require a similar amount of energy per unit of mass for full melting. While at the peak at 95°, the PCM stores more energy, it does not efficiently. The highest efficiency, measure as energy per unit of mass per melting time, follows the melting time curve (inverted): with the highest melting efficiency at $\theta = 45°$ at $L = 4\,cm$ and around $\theta = 0°$ for higher inclinations.

Regarding metrics on thermoconvective problems in fluids, there are two distinctive differences relative to the classic Rayleigh-Bénard (RB) problem. Firstly, the problem is transient; there is not an average in the long-time limit that suppresses the temporal term. Secondly, the latent heat term modifies the thermal dissipation which only depends on the melted phase. The evolving melting front scans a full range of Rayleigh numbers and allows to compare Nusselt, Reynolds numbers and thermal and kinematic boundary layers with those of Rayleigh-Bénard convection.

We find that the Nusselt number scales with Rayleigh as $Nu \sim Ra^{\alpha}$ for inclinations below the global bifurcation angle θ^c, and for a decreasing range of Ra with increasing the inclination for $\theta > \theta^c$. At small inclinations ($\theta \lesssim 10°$) the exponent decreases overall slightly with the inclination, with a more clear decrease with the size ($\bar{\alpha} = 0.25, 0.26, 0.27, 0.28$ for $L = 4, 6, 8, 10\,cm$). Higher inclinations lead to a trend of greater heat flux up to θ^c. At the laminar regime ($\theta > \theta^c$) there is a smooth decrease of α with the inclination. In addition, we find that the curve for $\theta = 45°$ has a higher area under curve than the rest. The higher value of integrated heat flux at $\theta = 45°$ explains the local (or global depending on size) minimum of the melting time curves at this inclination. Notice that this work uses 2D geometries, and from previous works on tetracosene melting in cubic geometries[31] is expected an enhancement of heat transfer in 3D, also is reported an enhacement of the Nusselt number in RB convection when 3D geometries support three dimensional flows[50]. How three-dimensional effects can modify the value of the exponents needs further investigation.

The Reynolds number also follows a power law $Re_v \sim Ra^{\beta}$ for $\theta \leq \theta^c$ and a wide range of Rayleigh numbers at the laminar regime. We have evaluated several definitions of the Reynolds number, and the definition based on the wing

Nomenclature

PCM	Phase Change Material		
Ra	Rayleigh number	Nu	Nusselt number
Pr	Prandtl number	T	temperature
Re	Reynolds number	f	liquid fraction
ρ	density	μ	dynamic viscosity
g	magnitude of gravity acceleration	p	pressure
$\hat{\mathbf{e}} = (\sin\theta, \cos\theta)$	unit vector	Γ	aspect ratio
Da	Darcy term	T_{ref}	reference temperature
α	thermal expansion coefficient	f_l	volume liquid fraction
$\mathbf{u} = (u_x, u_y)$	fluid velocity	C	Darcy coefficient
δ	tiny constant	H	thickness (domain size)
δh	latent heat	L	length (domain size)
T_h	temperature at the bottom wall	T_m	mean temperature
T_i	initial temperature at the solid state	Ste	Stefan number
h	averaged height of the melted PCM	t	time
Q_m	total input of energy per unit of mass	t_m	melting time
δ_u	thickness of the kinetic boundary layer	θ	angle
δ_T	thickness of the thermal boundary layer	θ^c	critical inclination
ϵ_u	kinematic dissipation rate	ν	kinematic viscosity
ϵ_T	thermal dissipation rate	η_k	Kolmogorov scale
T_s (T_l)	temperature in the solid (liquid) phase	η_b	Batchelor scale
c_s (c_l)	specific heats in the solid (liquid) phase	$J(y)$	vertical heat flux
λ_s (λ_l)	conductivity in the solid (liquid) phase		

velocity Re_v characterizes the effect of the inclinations with better fits to power laws. In contrast to the Nusselt number, we find that the exponent β decays strongly even at small inclinations. Thus, we find at non-inclination $\beta = 0.51, 0.50, 0.44, 0.39$ for $L = 4, 6, 8, 10\,cm$, and for a small inclination of $\theta = 1°$, $\beta = 0.44, 0.34, 0.36, 0.33$. The general trend of declining β with higher inclinations continues across the whole turbulent regime. At the laminar regime, we find as well a global trend of decaying β with the inclination.

The thickness of the thermal and kinematic boundary layers follow as well a power law when normalized with the average thickness of the melted phase $\delta_T/h \sim Ra^{\alpha_T}$, and $\delta_u/h \sim Ra^{\alpha_u}$. The exponent α_T is barely affected by small inclinations, similarly to α, with an averaged of $\bar{\alpha}_T = -0.24, -0.27, -0.27, -0.27$ for $L = 4, 6, 8, 10\,cm$ up to $\theta = 10°$. These values are not very distant from the -0.25 exponent predicted by the laminar Blasius-Prandtl boundary layer theory. On the other hand, the scaling of the kinematic boundary layer based on the wing velocity v is very slightly affected by very small inclinations $\theta \sim 1°$ contrary to the strong decrease of exponent β of Reynolds. At higher inclinations there is a strong decrease, from $\bar{\alpha}_u = -0.15$ at $\theta = 0°$ up to $\bar{\alpha}_u = -0.38$ at $\theta = 105°$. The exponent α_T does not exhibit a discontinuity at θ^c as the rest of exponents. It transitions from the turbulent to the laminar regime through gaining smoothness instead of a change of trend. An important effect of the inclination is that for $\theta > 10°$ progressively leads to the embedding of the kinematic boundary layer into the thermal boundary layer $\delta_u/h < \delta_T/h$.

Finally, we notice that to compare the results with the high Rayleigh literature, we have shown representations as a function of Rayleigh. However, representations based on the overall liquid fraction f_l, such as the threshold of stability of the base sate, secondary instability, Nusselt or Reynolds curves are more suitable to discern the effect of size and inclination.

ACKNOWLEDGMENTS

Authors thankfully acknowledge the support of the computer resources provided by ICMAT and by the Centro de Supercomputación y Visualización de Madrid (CeSViMa).

S.M. acknowledges support by the Spanish *Ministerio de Economía y Competitividad* under Projects No. TRA2016-75075-R and No. ESP2015-70458-P. J.C. acknowledges the support of the "Ramon y Cajal" project RYC2018-025169 and ICMAT Severo Ochoa Project SEV-2015-0554.

Data Availability Statement. Data available on request to the authors.

[1]R. Gulfam, P. Zhang, and Z. Meng, "Advanced thermal systems driven by paraffin-based phase change materials – A review," Appl. Energy **238**, 582–611 (2019).
[2]T. Xiong, L. Zheng, and K. W. Shah, "Nano-enhanced phase change materials (NePCMs): A review of numerical simulations," Appl. Therm. Eng. **178**, 115492 (2020).
[3]S. Madruga and J. Curbelo, "Dynamic of plumes and scaling during the melting of a phase change material heated from below," Int. J. Heat Mass Transf. **126, Part B**, 206 – 220 (2018).
[4]B. W. Webb and R. Viskanta, "Natural-convection-dominated melting heat transfer in an inclined rectangular enclosure," Int. J. Heat Mass Transf. **29**, 183–192 (1986).
[5]B. Kamkari, H. Shokouhmand, and F. Bruno, "Experimental investigation of the effect of inclination angle on convection-driven melting of phase change material in a rectangular enclosure," Int. J. Heat Mass Transf. **72**, 186–200 (2014).
[6]B. Kamkari and H. J. Amlashi, "Numerical simulation and experimental verification of constrained melting of phase change material in inclined rectangular enclosures," Int. Commun. Heat Mass Transf. **88**, 211–219 (2017).
[7]Y. Wang, J. Dai, and D. An, "Numerical investigations on melting behavior of phase change material in a rectangular cavity at different inclination angles," Appl. Sci. **8** (2018), 10.3390/app8091627.
[8]A. I. N. Korti and H. Guellil, "Experimental study of the effect of inclination angle on the paraffin melting process in a square cavity," J. Energy Storage **32**, 1–12 (2020).
[9]X. Yang, Z. Guo, Y. Liu, L. Jin, and Y. L. He, "Effect of inclination on the thermal response of composite phase change materials for thermal energy storage," Appl. Energy **238**, 22–33 (2019).
[10]J. Zhao, J. Zhai, Y. Lu, and N. Liu, "Theory and experiment of contact melting of phase change materials in a rectangular cavity at different tilt angles," Int. J. Heat Mass Transf. **120**, 241–249 (2018).
[11]R. Rabie, M. Emam, S. Ookawara, and M. Ahmed, "Thermal management of concentrator photovoltaic systems using new configurations of phase change material heat sinks," Sol. Energy **183**, 632–652 (2019).
[12]H. Zennouhi, W. Benomar, T. Kousksou, A. A. Msaad, A. Allouhi, M. Mahdaoui, and T. El Rhafiki, "Effect of inclination angle on the melting process of phase change material," Case Studies in Thermal Engineering **9**, 47–54 (2017).
[13]C. S. Ng, A. Ooi, D. Lohse, and D. Chung, "Vertical natural convection: application of the unifying theory of thermal convection," J. Fluid Mech. **764**, 349–361 (2015).
[14]R. Khalilov, I. Kolesnichenko, A. Pavlinov, A. Mamykin, A. Shestakov, and P. Frick, "Thermal convection of liquid sodium in inclined cylinders," Phys. Rev. Fluids **3**, 1–16 (2018).
[15]L. Zwirner and O. Shishkina, "Confined inclined thermal convection in low-Prandtl-number fluids," J. Fluid Mech. **850**, 984–1008 (2018).
[16]A. Baïri, N. Laraqi, and J. M. García de María, "Numerical and experimental study of natural convection in tilted parallelepipedic cavities for large Rayleigh numbers," Exp. Therm. Fluid Sci. **31**, 309–324 (2007).
[17]N. Williamson, S. W. Armfield, W. Lin, and M. P. Kirkpatrick, "Stability and Nusselt number scaling for inclined differentially heated cavity flow," Int. J. Heat Mass Transf. **97**, 787–793 (2016).
[18]I. V. Kolesnichenko, A. D. Mamykin, A. M. Pavlinov, V. V. Pakholkov, S. A. Rogozhkin, P. G. Frick, R. I. Khalilov, and S. F. Shepelev, "Experimental study on free convection of sodium in a long cylinder," Therm. Eng. **62**, 414–422 (2015).
[19]O. Shishkina and S. Wagner, "Prandtl-Number Dependence of Heat Transport in Laminar Horizontal Convection," Phys. Rev. Lett. **116**, 1–4 (2016).
[20]S. Weiss and G. Ahlers, "Effect of tilting on turbulent convection: Cylindrical samples with aspect ratio F = 0.50," J. Fluid Mech. **715**, 314–334 (2013).
[21]S.-X. Guo, S.-Q. Zhou, X.-R. Cen, L. Qu, Y.-Z. Lu, L. Sun, and X.-D. Shang, "The effect of cell tilting on turbulent thermal convection in a rectangular cell," J. Fluid Mech. **762**, 273–287 (2015).
[22]S. X. Guo, S. Q. Zhou, L. Qu, X. R. Cen, and Y. Z. Lu, "Evolution and statistics of thermal plumes in tilted turbulent convection," Int. J. Heat Mass Transf. **111**, 933–942 (2017).
[23]L. Jiang, C. Sun, and E. Calzavarini, "Robustness of heat transfer in confined inclined convection at high Prandtl number," Phys. Rev. E **99**, 1–10 (2019).
[24]Q. Wang, Z.-H. Wan, R. Yan, and D.-J. Sun, "Multiple states and heat transfer in two-dimensional tilted convection with large aspect ratios," Phys. Rev. Fluids **3**, 113503 (2018).
[25]S. Madruga and C. Mendoza, "Heat transfer performance and melting dynamic of a phase change material subjected to thermocapillary effects," Int. J. Heat Mass Transf. **109**, 501–510 (2017).
[26]V. R. Voller and C. Prakash, "A fixed grid numerical modelling methodology for convection-diffusion mushy region phase-change problems," Int. J. Heat Mass Transf. **30**, 1709–1719 (1987).
[27]V. R. Voller, A. D. Brent, and C. Prakash, "The modelling of heat, mass and solute transport in solidification systems," Int. J. Heat Mass Transf. **32**, 1719–1731 (1989).
[28]V. R. Voller, A. D. Brent, and C. Prakash, "Modelling the mushy region in a binary alloy," Appl. Math. Model. **14**, 320–326 (1990).
[29]S. Madruga and G. Mischlich, "Melting dynamics of a phase change material (PCM) with dispersed metallic nanoparticles using transport coefficients from empirical and mean field models." Appl. Therm. Eng. **124**, 1123–1133 (2017).
[30]G. Branch, S. S. Sebti, M. Mastiani, H. Mirzaei, A. Dadvand, S. Kashani, and S. A. Hosseini, "Numerical study of the melting of nano-enhanced phase change material in a square cavity," J. Zhejiang Univ. Sci. A **14**, 307–316 (2013).
[31]S. Madruga, N. Haruki, and A. Horibe, "Experimental and numerical study of melting of the phase change material tetracosane," Int. Commun. Heat Mass **98**, 163 – 170 (2018).
[32]B. I. Shraiman and E. D. Siggia, "Heat transport in high-Rayleigh-number convection," Phys. Rev. A **42**, 3650–3653 (1990).
[33]H. G. Weller and G. Tabor, "A tensorial approach to computational continuum mechanics using object-oriented techniques," Comput. Phys. **12**, 620–631 (1998).
[34]V. Voller and C. Swaminathan, "General source–based method for solidification phase change," Numerical Heat Transfer, Part B **19**, 175–189 (1991).
[35]H. J. Aguerre, S. Marquez Damian, J. M. Gimenez, and N. M. Nigro, "Modeling of Compressible Fluid Problems With Openfoam Using Dynamic Mesh Technology," Mecánica Computacional **XXXII**, 995–1011 (2013).
[36]S. Madruga and C. Mendoza, "Enhancement of heat transfer rate on phase change materials with thermocapillary flows," Eur. Phys. J. Special Top. **226**, 1169–1176 (2017).

[37]P. Subramanian, O. Brausch, K. E. Daniels, E. Bodenschatz, T. M. Schneider, and W. Pesch, "Spatio-temporal patterns in inclined layer convection," J. Fluid Mech. **794**, 719–745 (2016).
[38]J. E. Hart, "Stability of the flow in a differentially heated inclined box," J. Fluid Mech. **47**, 547–576 (1971).
[39]Y. M. Chen and A. J. Pearlstein, "Stability of free-convection flows of variable-viscosity fluids in vertical and inclined slots," J. Fluid Mech. **198**, 513–541 (1989).
[40]R. E. Kelly, "Mixed mode convection in an inclined slot," J. Fluid Mech. **246**, 545–568 (1993).
[41]R. Karami and B. Kamkari, "Investigation of the effect of inclination angle on the melting enhancement of phase change material in finned latent heat thermal storage units," Appl. Therm. Eng. **146**, 45–60 (2019).
[42]S. Madruga, H. Riecke, and W. Pesch, "Re-entrant hexagons in non-Boussinesq convection," J. Fluid Mech. **548**, 341–360 (2006).
[43]G. Ahlers, S. Grossmann, and D. Lohse, "Heat transfer and large scale dynamics in turbulent Rayleigh-Bénard convection," Rev. Mod. Phys. **81**, 503–537 (2009).
[44]B. Castaing, G. Gunaratne, F. Heslot, L. Kadanoff, A. Libchaber, S. Thomae, X.-Z. Wu, S. Zaleski, and G. Zanetti, "Scaling of hard thermal turbulence in rayleigh-bénard convection," Journal of Fluid Mechanics **204**, 1-30 (1989).
[45]S. Cioni, S. Ciliberto, and J. Sommeria, "Strongly turbulent Rayleigh-Bénard convection in mercury: comparison with results at moderate Prandtl number," J. Fluid Mech. **335**, 111-140 (1997).
[46]O. Satbhai, S. Roy, S. Ghosh, S. Chakraborty, and R. Lakkaraju, "Comparison of the quasi-steady-state heat transport in phase-change and classical Rayleigh-Bénard convection for a wide range of Stefan number and Rayleigh number," Phys. Fluids **31** 096605 (2019).
[47]G. Ahlers, E. Brown, and A. Nikolaenko, "The search for slow transients, and the effect of imperfect vertical alignment, in turbulent Rayleigh-Bénard convection," J. Fluid Mech. **557**, 347–367 (2006).
[48]S. Ciliberto, S. Cioni, and C. Laroche, "Large-scale flow properties of turbulent thermal convection," Phys. Rev. E **54**, 5901–5904 (1996).
[49]P. Wei and K.-Q. Xia, "Viscous boundary layer properties in turbulent thermal convection in a cylindrical cell: the effect of cell tilting," J. Fluid Mech. **720**, 140–168 (2013).
[50]A. Saxena, S. Singh, and A. Srivastava, "Flow and heat transfer characteristics of an open cubic cavity with different inclinations," Phys. Fluids **30** (2018), 10.1063/1.5040698.
[51]O. Shishkina, S. Horn, S. Wagner, and E. S. Ching, "Thermal boundary layer equation for turbulent Rayleigh-Bénard convection," Phys. Rev. Lett. **114**, 1–5 (2015),.
[52]L. Zwirner, R. Khalilov, I. Kolesnichenko, A. Mamykin, S. Mandrykin, A. Pavlinov, A. Shestakov, A. Teimurazov, P. Frick, and O. Shishkina, "The influence of the cell inclination on the heat transport and large-scale circulation in liquid metal convection," J. Fluid Mech. , 1–37 (2019).